Spatially Resolved Optical Measurements of Electron and Hole Spins in Monolayer Tungsten Diselenide

by

Spencer Batalden

A dissertation submitted in partial fulfillment
of the requirements for the degree of
Doctor of Philosophy
(Applied Physics)
in the University of Michigan
2021

Doctoral Committee:

Professor Vanessa Sih, Chair
Professor Steven Cundiff
Professor Cagliyan Kurdak
Professor Lu Li
Professor Theodore B. Norris

Spencer Batalden

bataspen@umich.edu

ORCID iD: 0000-0002-1844-836X

Acknowledgements

I would first like to thank my advisor, Vanessa Sih, for all of the help and encouragement provided over the course of my time here at the University of Michigan. She first introduced me to the world of spintronics and none of the work here would exist without her.

I also must thank all of the other members of the group who taught me much during our time spent in and out of the lab. I took my first steps into working with our experimental equipment with Dr. Marta Luengo-Kovac and Dr. Michael Macmahon. During my first few years in the lab, much of my time was spent working closely with Dr. Xinlin Song while initially constructing the experimental setup used throughout this dissertation. It's through our combined efforts that our apparatus was completed in its given form.

Many hours were also spent in and out of the lab conversing and learning with Dr. Joseph Iafrate, Howard Hsu, and Michael Dominguez. Our many discussions helped to deepen my knowledge and understanding of spin physics and how our experimental methods helped us learn about the world around us.

The work in this thesis could not have been completed without the help of members of Professor Jiwoong Park's group from the University of Chicago. Many samples were grown and characterized by Preeti Poddar, Baorui Cheng, and Fauzia Mujid. This work was supported by the U.S. Department of Energy, Office of Science, Basic Energy Sciences, under Award #DE-SC0016206.

Lastly, I of course need to thank my family and friends for always being there and their love throughout the years, no matter the time or place.

Table of Contents

List of Figures

Abstract

The development of spintronics devices over the last 30 years has necessitated study into a large number of unique semiconductors. In the past 8 years, one emerging focus of study has been into two dimensional materials, with a focus on layered Van der Waals materials such as graphene and transition metal dichalcogenides (TMDs). In this dissertation, we utilize optical methods to study the spatial dependence of the spin valley polarization in the monolayer TMD tungsten diselenide (WSe_2).

When reduced to a single monolayer, TMDs are a direct band gap semiconductor with large spin splitting in both conduction and valence bands. These materials also display valley-dependent optical selection rules, allowing for carefully tuned laser pulses to selectively excite electron and hole spins in one direction. We use time-resolved Kerr rotation and other similar optical methods to excite spin valley polarizations in monolayer MOCVD-grown WSe_2 and probe their dynamics. Our Kerr signal reveals bi-exponential decay with time constants of 100 ps and 3 ns. Measurements are repeated on multiple flakes with radii of approximately 9 to 13 micrometers, as well as more continuous sample areas with many overlapping grain boundaries. These measurements also reveal larger spin valley polarizations at the edges of individual flakes than near the centers. Both photoluminescence and reflectivity measurements are also performed on the same flakes, but do not exhibit a similar spatial dependence.

In order to perform the measurements described here, a time-resolved Kerr microscopy setup was constructed in our lab. This setup is capable of performing Kerr rotation measurements

while varying multiple parameters including pump-probe separation, pump-probe time delay, magnetic field, and spatial position on the sample. The pump and probe spot sizes on the sample using this experimental setup are under 3 microns FWHM, and the pulse width of the laser allows for time delay scans to be taken with 10 ps resolution. I was heavily involved in the assembly and calibration of this experimental setup; as such, its workings and calibration procedures are described in this dissertation.

Efforts were also taken to create electrically contacted samples in the Lurie Nanofabrication Facility. Multiple iterations of lithography procedures were performed in order to properly align source and drain contacts across sub-10 micron flakes. Unfortunately, once these devices were fully realized in the clean room, the lift-off procedure for the photoresist caused a significant drop in signal in the samples and therefore complete realization of these devices remains a promising subject of future work.

Chapter 1

Introduction

1.1 Motivation

Over the past 50 years, electronics have steadily gotten smaller and smaller while performing faster and faster. We are however quickly approaching the quantum limit of traditional CMOS architecture. One promising alternative to this traditional architecture is known as spintronics, which instead of using primarily the electron's charge to store data and process information also makes use of the electron's spin degree of freedom. The concept of "spin" was first proposed by Uhlenbeck and Goudsmit in 1925 [1], and using this additional degree of freedom allows for advantages over traditional electronics, providing possible increases in both computational speed and energy efficiency [2,3].

The birth of modern spintronics is often attributed to the discovery of giant magnetoresistance (GMR) in 1988 by Fert and Grunberg, who were awarded a Nobel Prize for their work in 2007 [4,5]. GMR is an effect present when ferromagnetic and non-ferromagnetic materials are arranged in alternating layers. Spin-dependent scattering in the interfaces between layers causes a 'giant' change in the electrical resistance of these layers dependent on whether the adjacent ferromagnetic layers are parallel or antiparallel in their alignment. In practice, this means the resistance of the material can be controlled by an external magnetic or electric field,

depending on the desired method of control. In this way, GMR has found wide usage in commercially successful spintronic devices, including the read heads for hard drive disks found in many modern computers as well as magnetic RAM [6].

However, much present-day spintronic research has instead turned towards many types of semiconductors. Semiconductor-based spintronic devices have the advantages of providing control over the properties of the electrons within the device such as the density, as well as being much easier to integrate with existing semiconductor-based electronics. Even more recently, the discovery of graphene in 2004 by Geim and Novoselov has led to a massive spike in interest in the capabilities of 2-D materials, as evidenced by their Nobel prize awarded in 2010 [7]. One variety of materials that came forward in this increased interest is that of transition metal dichalcogenides (TMDs). These materials combine the two-dimensional thinness of graphene with optical selection rules that allow for all-optical electron spin generation within the material. This dissertation will focus on electron spins in one particular TMD, tungsten diselenide (WSe_2), and the experimental apparatus constructed in order to study such materials.

1.2 Outline

To begin this dissertation, we will first discuss the electronic and optical properties of TMDs which make them interesting prospects for spintronic devices in Chapter 2. We will view how they transition from indirect gap semiconductors in the bulk to direct gap once only a single layer exists as well as the origin of their spin-based optical selection rules. In Chapter 3, we will then discuss the experimental methods primarily used in the lab to interact with and study these materials. The primary focus will be on time-resolved Kerr rotation (TRKR) and variations on this technique. Chapter 4 will go on to introduce an experimental setup that was constructed in order to perform TRKR and photoluminescence measurements with micron-scale spatial

resolution. We will explain how this setup was developed and calibrated, as well as its capabilities for investigating spatially inhomogeneous samples, as well as spin polarization drift and diffusion. Chapter 5 will then focus on the WSe_2 device fabrication process that underwent many revisions in the Lurie Nanofabrication Facility and the current results of that process. In Chapter 6, we will show some of the results obtained using the experimental apparatus by showing measurements of spatially-resolved photoluminescence, TRKR, and pump-probe spatial overlap scans that can characterize spatial variations observed in MOCVD-grown monolayer WSe_2 which were recently published in *Optics Express* [8].

Chapter 2

Introduction to TMDs

2.1 Introduction

In this chapter, we'll get our first look at the samples studied in this dissertation. We'll look at the transition metal dichalcogenide crystal structure, as well as how the electronic band structure depends on the number of layers that these materials have. We will then take time to understand the optical selection rules that make these materials useful for optoelectronics and spintronics purposes as well as why they are attractive for an optics lab to study.

2.2 Crystal Structure

Bulk transition metal dichalcogenides (TMDs) are semiconductors with indirect band gaps of around 1-2 eVs. These materials are layered in nature, meaning that they are made up of many layers, with strong intralayer ionic-covalent bonding and much weaker interlayer Van der Waals bonds [9]. They follow the chemical formula MX_2, with M being a transition metal usually Molybdenum or Tungsten, and X being a chalcogen (group 16 on the period table) usually Sulfur, Selenium, or Tellurium. Each layer of these materials consists of one plane of transition metal atoms sandwiched between planes of chalcogen atoms. In the bulk, these semiconductors have an indirect band gap. However, multiple changes happen as these materials

are thinned to fewer and fewer layers, with the most interesting changes occurring when the material exists as a single monolayer.

The weak Van der Waals forces between layers make it possible to realize monolayers of these materials fairly simply. The scotch tape method allows mechanical exfoliation to often result in islands of single layers of layered materials to be readily available for study. The usage of this technique was first widely utilized in the study of graphene, but can be expanded to any other Van der Waals material. This also extends to the possibility of tuning growth techniques to produce areas of monolayers as well.

As fewer and fewer layers of a TMD are taken, the band structure of both the conduction and valence bands change. Where there is originally an indirect gap from the gamma point of the valence band to another point in the conduction band, a decrease in layers raises the energy of the K point to above that of the gamma point in the valence band while simultaneously decreasing the energy of the K point in the conduction band. Only once the TMD has been decreased to a single layer do both of these changes cause the band gap to become a direct gap at the K point [10]. This has been experimentally verified via an orders of magnitude increase in photoluminescence intensity at a monolayer as compared to even bilayer materials [11].

2.3 Optical Selection Rules

In addition to the change from indirect to direct band gap at the monolayer transition, there is also an emergence of useful optical selection rules. At the monolayer, TMDs no longer have spatial inversion symmetry. This lack of spatial inversion symmetry gives rise to valley-selective circular dichroism. That is, there are two separate types of K valleys in these materials, K+ and K-, that each interact with a different helicity of light. While the inversion symmetry argument only works for precisely the K points, in practice the entire valleys show large amounts

of circular dichroism, only changing sign rapidly at valley boundaries. These valley-dependent optical selection rules are interesting on their own, but are even more interesting when paired with the large spin splitting that also occurs at the K+/- valleys. This large spin splitting of around 400 meV in the WSe_2 and 200 meV in the $MoSe_2$ valence bands occurs due to the strong spin-orbit coupling of TMDs from the presence of the transition metals [12]. A band structure diagram with the optical selection rules and spin splitting can be seen in Fig. 2.1. Time reversal symmetry also requires that this spin splitting have opposite sign between the K+ and K- valleys. This splitting occurs in both the conduction and valence bands; however, the magnitude of the splitting is much larger in the valence than in the conduction band.

The combination of valley-dependent optical selection rules and the opposite spin splitting between the two valleys means that if circularly-polarized light of the appropriate energy range is used, electrons and holes can be excited in these materials that are in a known valley with a known spin. Thus, at these wavelengths there exist spin-dependent optical selection rules.

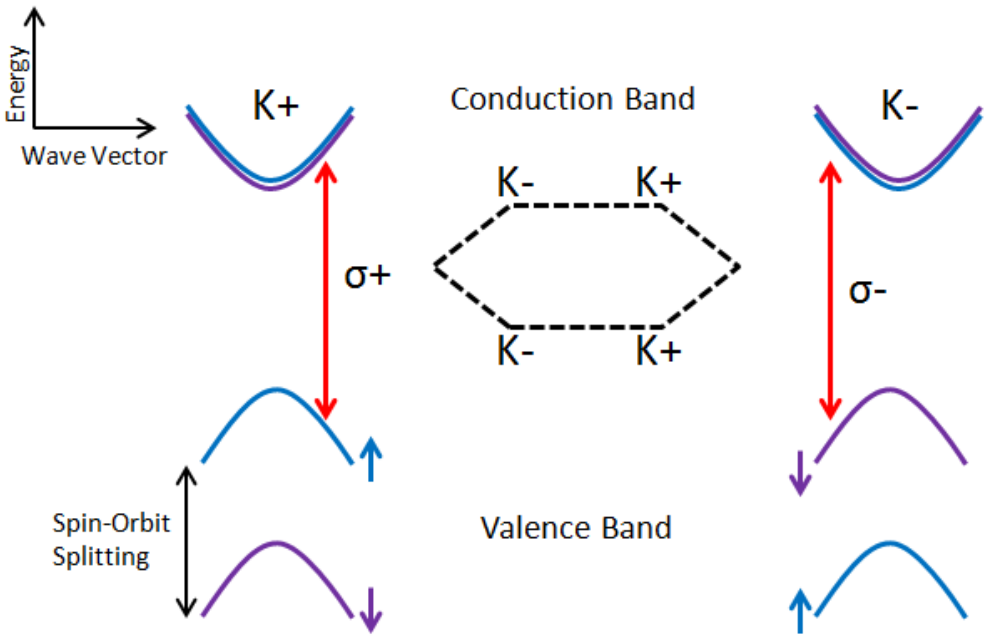

Figure 2.1 Band Diagram of Tungsten Diselenide
The lack of inversion symmetry of TMDs leads to a discernible difference between the K+ and K- valleys. Spin-orbit splitting exist in both the valence and conduction bands of these materials, with the valence splitting being hundreds of meV. These splitting have opposite signs between K+ and K- valleys. Additionally, circularly polarized light interacts with individual valleys, with right circular polarization interaction purely with the K+ valley and left with the K- valley.

2.4 Conclusion - Why TMDs?

While sub-optimal for optical experimentation in bulk, these materials have both a direct band gap and spin valley-dependent optical selection rules as monolayers. In addition, the weak Van der Waals forces mean that these monolayers can be relatively easily created via various means, both mechanically and through growth processes. The two-dimensional nature of these materials also leads to large exciton binding energies and allows for them to be used as “building blocks” for heterostructures created with other Van der Waals materials, most notably graphene. These heterostructures can combine useful properties of multiple materials, i.e. spin generation from TMDs and transport properties of graphene, with large exchange interactions because of

their close proximity from being single layers. In addition, the spin-orbit splittings that exist in both the conduction and valence bands even in the absence of external magnetic field result in long spin valley coherence times [13]. Therefore, it is useful to understand transition metal dichalcogenides for future usage in spin valleytronics.

2.5 Overview of Previous Work

Looking at these reasons for transition metal dichalcogenides being an exciting classification of materials for research, it should come as no surprise that in the past decade they have been the subject of much research and discussion over the past decade [14,15]. Due to the multiple methods available to create samples of monolayer TMDs, large variations from sample to sample are present in published research. Measurements of spin lifetimes have orders of magnitude variation depending on how the sample was created (exfoliated vs. grown) and even within the different techniques themselves.

When exfoliation has been used to create these monolayers, lifetimes can vary from 2 ns [16] to 150 ns [17], even up to 2 μs [18], depending primarily on the cleanliness of the created sample and encapsulation used to protect the monolayer from outside influences. However, in this dissertation we will be performing experiments on MOCVD-grown WSe_2, which more typically has had measurements of spin valley lifetimes from 10 ps [19], in the case of electron spins, to 80 ns [13]. Our experiments, reporting measurements of biexponential decays with the two lifetimes around 100 ps and 3 ns, fit near the middle of the lifetime range currently being seen in grown TMDs.

The intrinsic valley lifetime in these materials is expected to be much longer than these current measurements [20,21], however in grown materials especially, the presence of defects strongly limits the maximum experimentally verified lifetimes. The origin of the long lifetimes in

these materials is, in the end, not well understood. Some previous studies attribute the longest lived lifetimes to resident electrons and holes [19,22,23], while others attribute them to dark trions [17].

After a circularly-polarized pumping laser pulse strikes a TMD sample, depending on the energy of the laser there are initially bound excitons or trions residing in either the K+ or K- valleys. This initial state rapidly decays, giving rise to a few hundred picosecond lifetime [24,25] seen in many studies [8,13,16,26]. However, what happens immediately after this has been the subject of much discussion. One school of thought is that these excitons/trions all immediately recombine, after having interacted in some way with the resident carriers, passing their spin onto the carriers. In this way, it is purely the spin polarization of the resident carriers themselves left over from their interactions with the excited excitons that is the cause of the lifetimes measured in TMD monolayers. The other train of thought is that the bright trions initially excited by the pump laser pulse do not all recombine, but instead some population decays into dark trionic states. These so-called dark states are so named due to their inability to radiatively recombine. The remaining electrons and holes in the trion exist in different states such that their recombination would violate spin conservation. These dark trions would only be long-lived in TMDs with spin splittings in the conduction and valence band such that the opposite spins of electrons and holes are the lowest energy bands, as is the case for WSe_2 which we study in this dissertation.

The field of research into transition metal dichalcogenides has had much attention paid to it since these materials were first brought to the forefront nearly a decade ago. Despite this, or perhaps because of this, there are still open questions and debate about the exact origin of the

long-lived spin signals that have been measured as well as just how long these lifetimes may be able reach, with longer lifetimes being reported every year.

Chapter 3

Introduction to Experimental Methods

3.1 Introduction

In this chapter, we will begin looking at the primary experimental technique used in our lab, time-resolved Kerr rotation. We will get our first look at the experimental apparatus used to perform these measurements as well as how they help us view the electron dynamics in semiconductor samples.

3.2 Kerr and Faraday Rotation

As explained previously, striking transition metal dichalcogenide samples with a circularly polarized laser pulse will produce a spin valley polarization. This is caused by valley-dependent optical selection rules for right and left circularly polarized light and opposite spin splitting in the valence and conduction bands of the K+ and K- valleys. Once we have this spin valley polarization, it is necessary to probe the sample in some way in order to understand how the spin valley packet is behaving, both spatially and temporally. Because some circularly polarized light has been absorbed and excited spins in one set of valleys, the Fermi energy of one set of valleys has risen above that of the other. This causes a difference in absorption for the two handednesses of light, known as circular dichroism. Using the Kramers-Kronig relation, this can

be used to additionally calculate a difference in refractive index for left and right circularly polarized light (circular birefringence).

In our experiments, we direct two laser beams to the sample: a circularly polarized pump beam and a linearly polarized probe beam. We have now seen that the initial pump beam will cause the material to exhibit circular birefringence for as long as a spin valley polarization remains in the sample (a time which depends on the spin valley lifetime of the sample). The linearly polarized probe beam can be rewritten as a superposition of left and right circularly polarized beams. Because the two circular polarizations of light experience different refractive indices when striking the sample, different phases are imparted to these portions of the beam upon reflection. When we then recombine the left and right circularly polarized light into a single linearly polarized beam, a shift between their phases will appear as a rotation of the angle of linear polarization. This rotation of the linear beam is known as the magneto-optic Kerr effect, due to first being demonstrated by John Kerr in light reflected from a magnetized surface. The angle of rotation itself (compared to the linear polarization were there no circular birefringence) is called the Kerr angle. Larger spin valley polarizations will cause proportionally larger Kerr rotation angles.

When light strikes a sample and is reflected off, some is of course transmitted instead of being reflected from the surface of the sample. This transmitted beam can then be reflected off the back of the sample instead of the front and as such has travelled through some small amount of the sample. Because of this, we should also spare a moment to think about what happens to the probe beam as it is transmitted through this material. Once again, we recall that the pump beam caused our sample to exhibit circular birefringence. This means that if we once again decompose probe beam into the two circular polarizations, they will travel at a different speed

through our sample. This difference in speed will be evidenced by a phase shift between the two polarizations upon exiting the sample, once again manifesting as a rotation of the linearly polarization of the probe beam. This rotation, known as Faraday rotation, was originally found in 1845 by Michael Faraday, 30 years before Kerr rotation was first discovered. However, this angle is once again proportional to the spin valley polarization present in our samples. Thus, the angle that our probe beam is rotated after either being reflected by or transmitted through the sample will still be proportional to the spin valley polarization as a whole and can be used as a way to measure the spin valley dynamics in our sample after excitation.

3.3 Time-resolved Kerr Rotation

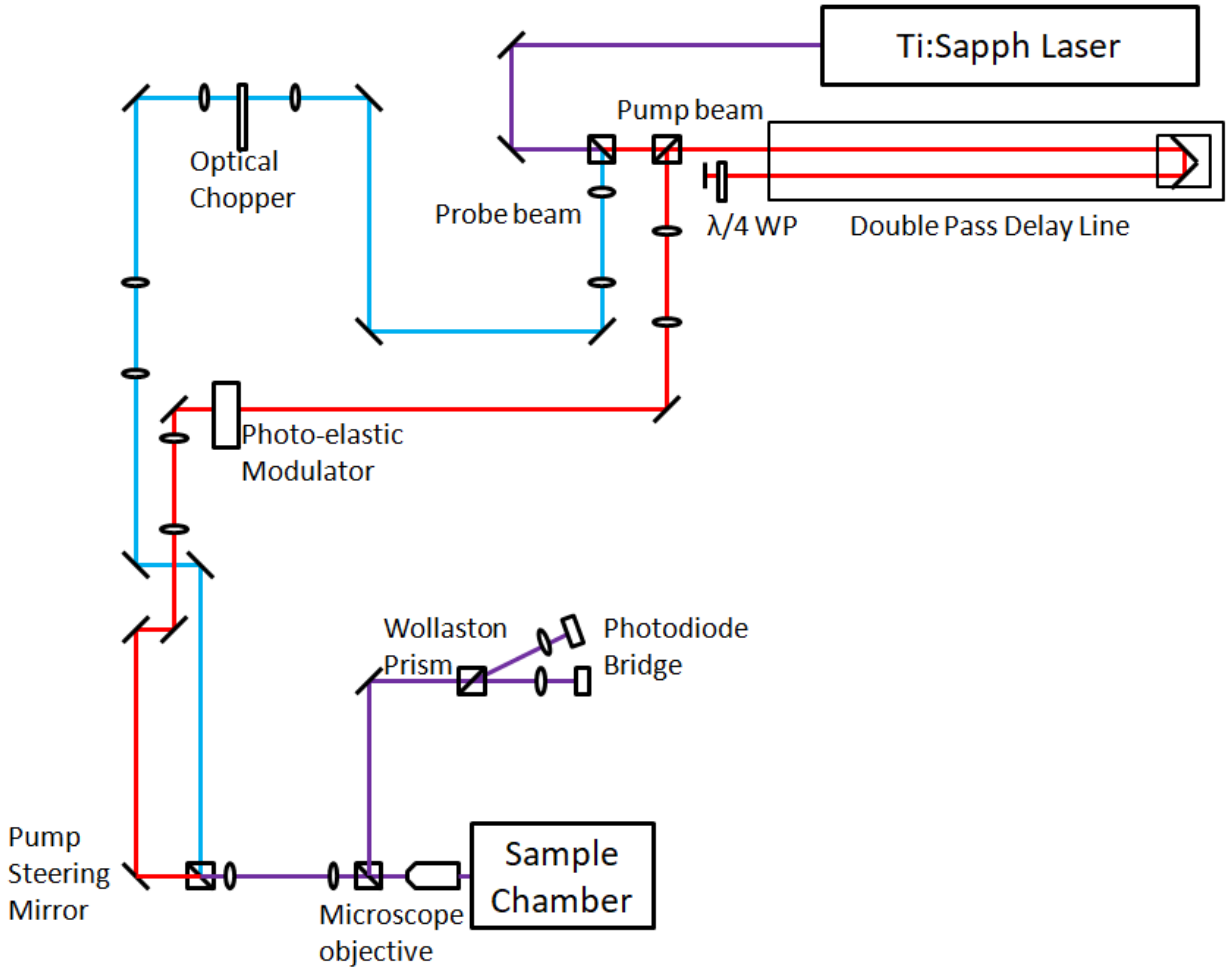

Figure 3.1 Kerr rotation setup
Overview of the TRKR setup created for and used in this dissertation. Pump and probe paths can be traced through the setup, with the pump modulated with a photo-elastic modulator and passing through a delay line and the probe modulated by an optical chopper. The pump can additionally be directed relative to the probe by the motorized mirror. Multiple pairs of collimation lenses are included to maintain pump and probe beam collimations throughout the apparatus.

Time-resolved Kerr rotation (TRKR) is a powerful experimental technique that can be used to probe electron spin dynamics in different species of semiconductors. To enable the high temporal resolution necessary to measure nanoseconds-long decay times, it is necessary to utilize a pulsed laser. Our lab uses a Coherent Mira 900 Ti:Sapphire laser which produces picosecond

pulses at a repetition rate of 76 MHz, translating to 13.16 nanoseconds between pulses. These pulses are split by a beam splitter into pump and probe beams and then directed through various optics to the sample. The pump beam is directed through a photoelastic modulator (PEM), which takes the originally linear beam and causes it to oscillate between left and right circularly polarized light at 50 kHz. This allows us to feed the final signal into a lock-in amplifier at this frequency to increase the signal-to-noise ratio. Likewise, the probe beam has an optical chopper positioned at the focus of a collimating lens pair to provide a second lock-in amplification frequency. The cascading lock-in technique is discussed later this chapter.

We understand what will occur when one of our samples is struck by a circularly polarized pump beam followed by a linearly polarized probe beam; the probe beam will be rotated by an angle proportional to the remaining spin valley polarization. When the two beams are being directed to the sample, the pump beam is sent down a motorized delay line as shown in Fig. 3.1. This delay line is aligned such that when the retroreflector at the end is moved, the outgoing pump beam experiences no change in position or angle, only a change in path length. Because we know the speed at which light travels, this change in optical path length causes the pump pulse to reach the sample at a different time when compared to the probe pulse. Mechanical control of the delay line then enables us to choose a specific time delay between pump and probe pulses reaching the sample, allowing the spin valley dynamics at different times to be measured.

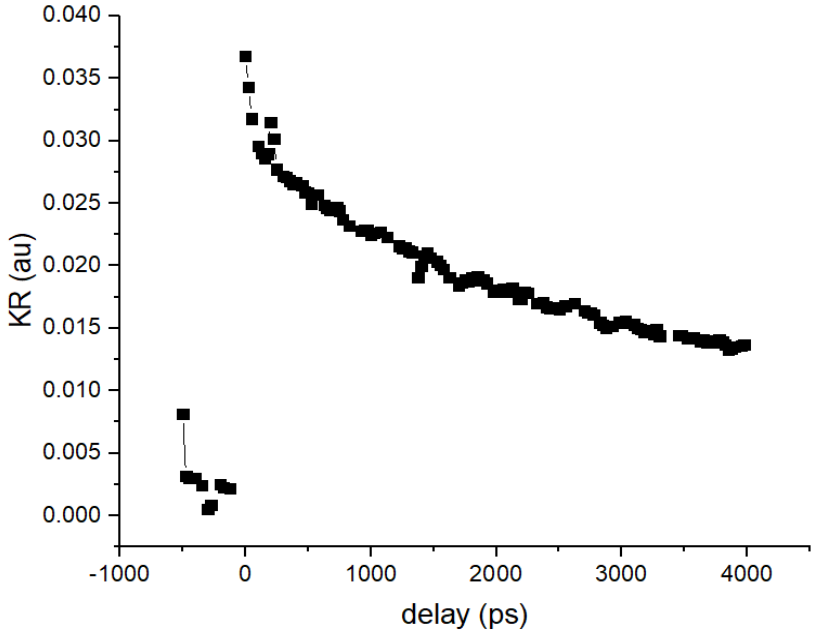

Figure 3.2 Sample TRKR curve of WSe_2
This data was taken at 10 K, with 2.4 mW pump power and 0.4 mW probe power at 742.5 nm laser wavelength. The signal remains from the previous pump pulse, which would have occurred at -13160 ps.

A representative TRKR curve can be seen in Fig. 3.2, showing a decrease in spin valley polarization with time and allowing us to fit with an exponential decay curve to determine the lifetime of spins in our sample. Some signal at negative time delay can be seen in the TRKR graph. This corresponds to the probe pulse striking the sample before the corresponding pump pulse has reached it. However, because our laser has a repetition rate of around 13.1 ns, the negative delay can also be viewed as arriving after a large positive delay from the previous pump pulse, in our case by adding 13,160 ps to the time delay. It is useful to include a small amount of negative delay signal in TRKR experiments as this can provide a baseline for the signal, i.e. what the signal looks like after a long time. In the scan shown, the lifetime of our spin valley signal is around 3 ns, so a very small amount of signal should be remaining at the negative (13000 ps) time delay. It is possible for samples of materials worked with here (WSe_2) to exhibit lifetimes

longer than our maximum time delay, meaning that a decaying exponential would have difficulty providing a dependable fit due to viewing such a small part of the decay. In this case, there are other methods for determining the decay time [13, 27]. However, none of the samples described in this work have a decay constant that match or exceed the repetition period of our laser, and as such we will not describe these methods here.

3.4 Spatial Overlap

In addition to control over the time delay between pump and probe pulses, the experimental setup described in this dissertation can also control the relative position at which the two pulses strike the sample. In typical TRKR scans as shown in Fig. 3.2, the pump and probe beams have been directed to strike the sample at the same position so as to provide the greatest amount of signal. The probe beam is only able to measure the spin valley polarization where it strikes the sample, and as no electric field is applied the greatest signal should generally be at the point where the pump beam is positioned. However, control over their relative positions can still be a powerful experimental technique. In our setup, a motorized steering mirror is placed in the pump beam's path, allowing it to be redirected and scanned in two dimensions over the probe beam.

We can reasonably assume that both pump and probe pulses have Gaussian shapes when travelling through the air. Once the beams have been focused onto the sample then, it can be assumed that their intensity profiles on the sample surface remain roughly Gaussian. When the pump spot is scanned laterally over the probe spot while keeping the time delay between the pulses fixed, the shape of the resulting curve will be a convolution of the two intensity profiles. Fortunately, the convolution of two Gaussians remains a Gaussian itself with variance equal to the sums of the variances of the original two curves. This means we can fit the resulting curve

with a Gaussian to obtain a measure of the width of our spin valley packet, as seen in Fig. 3.3. The real power of this technique however, comes when we combine it with the control over time delay that we also have. These pump-probe spatial overlap scans can be performed at multiple fixed delay times, providing accurate measures of both the signal amplitude and width at each time delay. The amplitudes at each time delay can be fit as another measure of spin valley lifetime in the sample, although this would not be expected to change from the direct TRKR fit. The widths provide additional physical insight however, giving a measure of the spin valley diffusion. Any change in the width of the spin packet over our available time delays would have to be caused by diffusion of the packet over time.

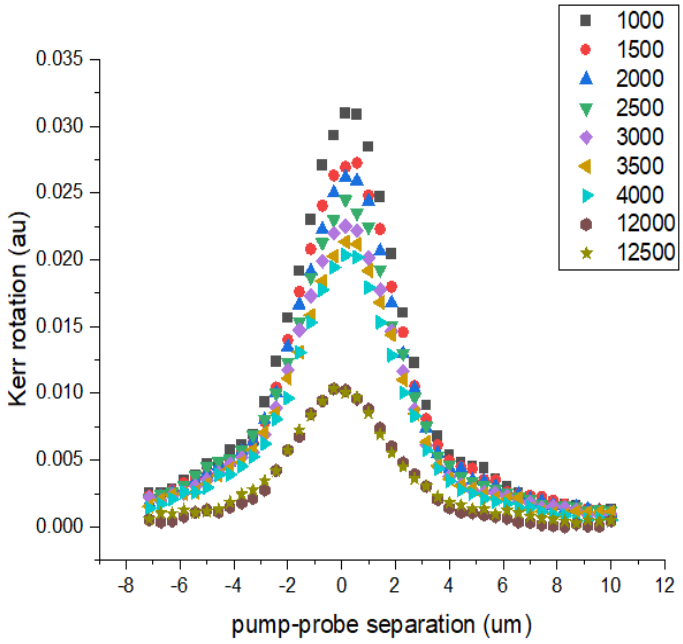

Figure 3.3 Sample pump-probe overlap scan
This data was taken at 10 K, with 2.4 mW pump power and 0.4 mW probe power at 742.5 nm laser wavelength. Dots represent raw data from multiple overlap scans from differing time delays. Each time delay is fit using a Gaussian distribution to extract the amplitude and width of the overlap scans.

3.5 Cascading Lock-in Amplifiers

Because the angles exhibited by Kerr rotation in our samples are small, on the order of microradians, great care must be taken to achieve a high enough signal-to-noise ratio to extract these small angles. The first step taken in this respect is the utilization of a balanced photodiode bridge at the end of the path which collects the reflected pump and probe light. What we are ultimately interested in is any change in the linear polarization direction of the probe light occurring at both the frequencies of the pump and probe modulations. To best determine a small change in a signal, it is ideal to start with a small signal for the relative change to be large. The best way to do this is to direct the collected beam through a Wollaston prism, which refracts the vertical and horizontal components of the light in different directions. We collect the split beam with two photodiodes and direct their output through a bridge which takes their difference. This means that we can utilize a half wave plate in the probe beam path to rotate the non-Kerr rotated beam such that it is at a 45-degree angle with the table. This means equal intensities will be directed down each path past the Wollaston prism, causing the initial signal to be zero. Thus any non-zero signal can be attributed to a rotation of the probe beam.

The next steps taken to increase the signal-to-noise ratio even more are the pump and probe modulation frequencies introduced earlier. The pump is modulated at 50 kHz by a PEM while the probe beam uses an optical chopper with a much smaller, sub 1 kHz frequency. To determine whether we have any signal happening at both frequencies, we must use a cascading lock-in amplifier setup. This arrangement of electronics allows for the output of one lock-in amplifier to be supplied to the input of a second. In this way, the original signal from the diode bridge can be filtered down to just the portion that is changing at both pump and probe

frequencies [27]. This leads to a large signal-to-noise ratio, which is necessary for extracting microradian Kerr rotation angles.

Chapter 4

Construction and Documentation of Experimental Apparatus

4.1 Introduction

A large portion of my time at the University of Michigan was spent creating and optimizing a Kerr microscopy setup for our lab. As I spent so much time working with it and have taken it through multiple iterations to achieve the successes with it that we have today, it feels necessary to include this longer chapter going into more detail on the experimental setup itself as well as all the work that went into getting all the individual pieces calibrated and aligned and working together in concert. As such, here we will be exploring in more detail the 4-f setup employed to enable our pump-probe overlap scans, the piezoelectric stages housed within the cryostat itself that allow the sample to be positioned and scanned, and the electromagnet which is also housed in the sample chamber, as well as the calibration that was necessary. Additionally, it is easy for much of the useful working knowledge to be lost when the graduate student who worked most with a new setup leaves the lab, to only be roughly reconstructed by reading through lab notebooks and dissertations. I will also in this chapter be leaving a more thorough window into the day-to-day running of this setup that will be useful to future students coming into the Sih lab and hoping to make use of everything that has been put together and is available

to them. This will involve a slightly closer look at techniques used for mounting and wiring samples used in this cryostat, as it is fairly unique in our lab, as well as some problems that have been troubleshot in the past and have a higher than average likelihood of occurring again at some point in the future.

4.2 TRKR Setup

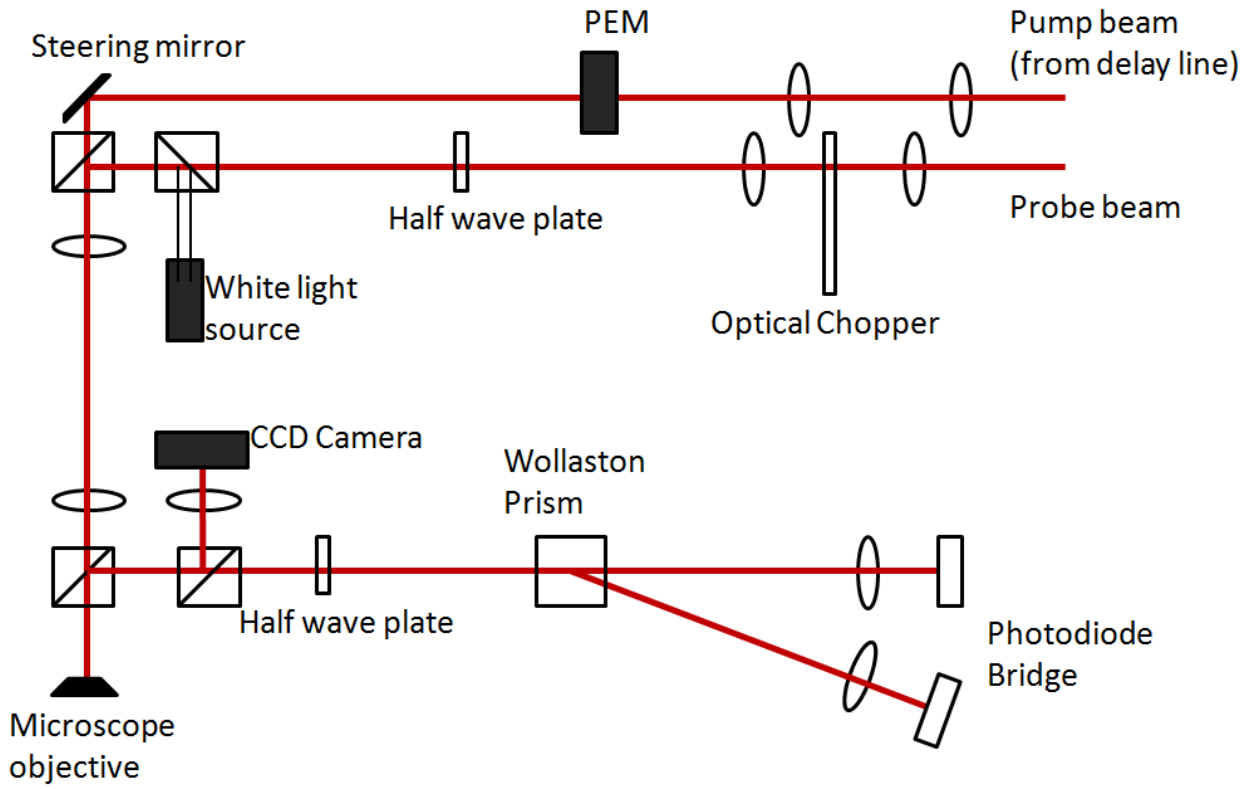

Figure 4.1 Kerr rotation setup near the sample chamber
Both pump and probe beams have traveled 5+ meters before arriving at the microscope objective focused onto the sample. The pair of lenses at the beginning of each path shown here maintain the collimation of the beam, with the probe beam also being chopped at the focus to give the most square wave-like chopping pattern. A white light source is joined with the probe path via a beam splitter to illuminate the sample and allow location of sample features by viewing the image formed on the CCD which is split off from the collection path with an additional beam splitter. The inclusion of beam splitters as compared to flip mirrors allows the beam position on the sample to be monitored during data collection at the cost of beam power.

Time-resolved Kerr rotation (TRKR) has been used in the Sih lab for many years on multiple setups, but we now want to perform studies on a much smaller length scale than has been previously accomplished. Historically, the TRKR setups have used large lenses to focus the pump/probe laser down to ~40 um spot sizes which is more than small enough for usage on homogeneous, millimeter sized samples. We now wish to perform spatial studies on 10 um TMD flakes, meaning that a resolution a full order of magnitude smaller than previously used is necessary. To accomplish this, a 50x microscope objective with a numerical aperture of 1.4 is focused on the sample in a new Montana Instruments cryostation that allows for the objective to be positioned within its 15 mm focal length of the sample mount. A complete schematic of the setup we constructed can be seen in Fig 4.1. The inclusion of a microscope objective in contrast to previously used lenses led to additional difficulties in establishing a working setup, along with learning to work with a new type of cryostat.

When performing TRKR measurements, the reflected probe beam needs to be collected and directed to a photodiode bridge. Typically the pump laser beam enters the lens focusing on the sample off-axis and so its reflection can be blocked prior to entering the collection path. However, this setup utilizes a microscope objective with an aperture only slightly larger than the pump/probe laser profile. Any separation that could be achieved between the beams, however small, would cause them to be near the very edges of the aperture, leading to imperfect beam shapes (stretched, cut off) striking the sample. Therefore, any light entering the objective that we wish to strike the sample at the same spot as the probe will also end up gathered and brought to the end of the collection path and thus the photodiode bridge. So in most experiments where our pump and probe strike the sample at the same place, both pump and probe beams are being collected and their signals are sent to the cascading lock-in amplifiers. The pump/probe powers

that were found to give the best results and so were used for most experiments were 2.4mW/.4mW, meaning there is much more pump than probe light being collected. Combined with the first amplifier locked in to the pump frequency, there is concern for the pump signal to leak into our final data.

To mitigate this concern, an additional half-wave plate is introduced into the setup in the probe path prior to being combined with the pump beam and sent into the objective. This wave plate, combined with the half-wave plate directly in front of the Wollaston prism, allows us to balance both the pump and probe beams on the diode bridge. Previously, just the second wave plate was necessary to balance the probe beam on the bridge, but with two beams to balance a second wave plate that only affects one of the beams is necessary. If the pump beam were purely circularly polarized, the Wollaston prism would direct half of the light to each side of the diode bridge and the pump would always be balanced. Unfortunately, the pump beam is being modulated between right- and left-circularly polarized light by the PEM and so there is an additional 50 kHz signal from the bridge as a result of the pump laser. The half wave plate directly in front of the prism allows that signal to be adjusted, but not removed completely. With a correctly chosen angle, the pump-dependent output from the bridge can be reduced to a 100 kHz (2f) oscillation on top of a DC offset. While not as good as removing the pump beam entirely from the equation, this allows the first, pump frequency lock-in to already filter out a majority of this pump signal, to the point where there is no noticeable noise from the pump beam after the cascading lock-in.

4.3 4-f Setup

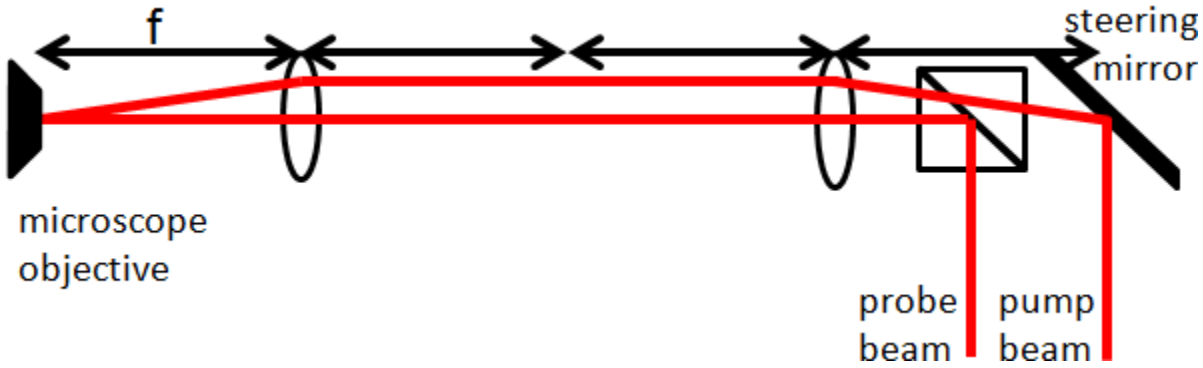

Figure 4.2 4-f Setup
The pump and probe beams are steered through this lens pair, causing both beams to enter the center of the microscope objective. The pump beam can then be directed relative to the probe using the steering mirror with no loss of coupling into the objective.

Another concern arising from the small aperture is the ability to perform spatial overlap scans. In order to move the pump spot relative to the probe spot on the sample, a motorized scanning mirror is used to adjust the angle at which the pump beam enters the microscope objective. The size of our scanning window is determined by how far the beam can be moved before it begins clipping on the edge of the aperture. The steering mirror must be placed as closely as possible to the objective to obtain the largest possible angle with a minimal change in where the pump strikes. However, this steering mirror must also be placed before the pump and probe beams are combined as well as before the beam splitter that splits the collection path out from the incoming beams. On top of this, the cryostat is constructed in such a way that the optical path must enter from above to reach the sample. The height this occurs at is much higher than the height that the laser is kept at on the optical table (The laser beam is maintained at the height that it is originally created at in order to best preserve the pulse shape/polarization.). So

there's also a periscope directly before the microscope objective since the objective must be entered from higher above the table than we would like to have optics positioned in the interest of stability. In practice, this means that the pump steering mirror ends up a large distance from the microscope objective. This decreases the pump-probe overlap scanning window appreciably, to the point where it is unable to separate the pump and probe beams enough for overlap studies to be performed.

To solve this, we utilized a 4-f geometry as shown in Fig. 4.2. This configuration utilizes a pair of planes that are four focal lengths apart where any light directed through the plane and into the first lens will exit the final plane at a position and angle reflected across the shared optical axis. By placing a motorized steering mirror which the pump beam strikes on the optical axis at the first plane and the microscope objective that focuses light on our sample at the final plane, the pump beam can be directed to enter the objective across a wide range of angles without any change in the laser power incident on the sample that would otherwise be caused by clipping on the objective. Once through the objective, this range of angles translates to a range of positions on the sample that are then used to perform pump-probe spatial overlap scans by scanning the pump spot across the probe. The additional benefits of this 4-f setup can be seen in Fig. 4.3, showing the increased visible area of samples held in the cryostat when illuminated by a white light source.

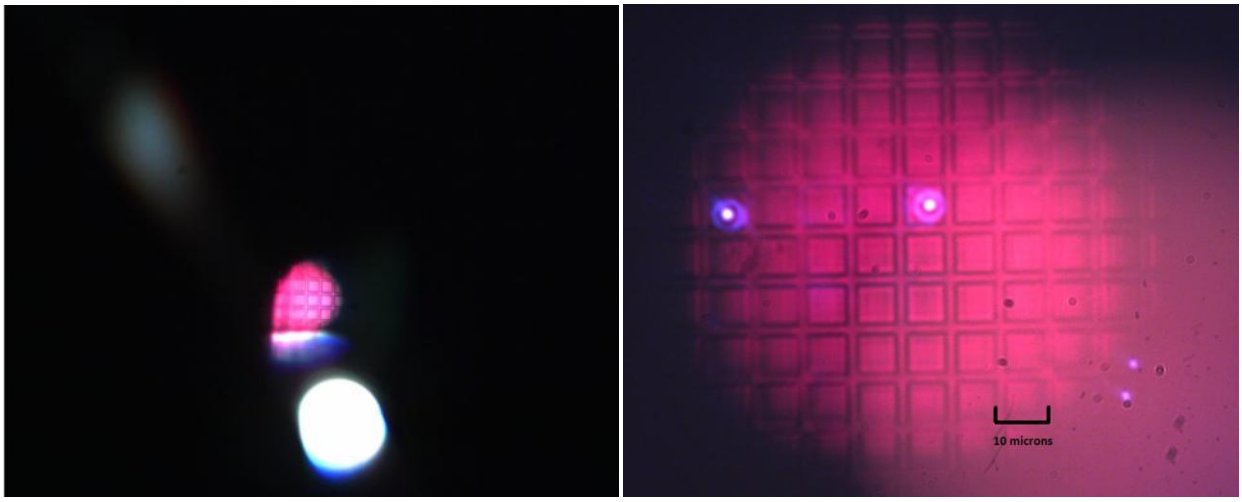

Figure 4.3 Imaging success of 4-f setup
Photos taken of the calibration sample when placed within the cryostat before and after the inclusion of the 4-f geometry. The zoom of the photo is simply a function of where white light optics were able to be placed relative to the sample, but the much larger visible area is necessary to view samples and locate 10 micron grains present on much larger substrates.

4.4 Working with the MI cryostat

The Montana Instruments cryostation used in the construction of this setup is new to the lab and behaves differently from other cryostats previously used. As such, this part of the chapter will go through usage of its multiple features and how to troubleshoot problems that have occurred/may occur again in the future. This cryostat is a closed-cycle helium cryostat, meaning that it does not require additional liquid helium to cool down to cryogenic (< 10 K) temperatures, but instead collects and recompresses the helium that it uses in a closed loop. As such, it is simpler to cool down/warm up than helium flow cryostats at the cost of additional power consumption and time used. When cooling the cryostat down from room temperature, around 3 hours should be given for it to pump down to high vacuum and reach the target temperature. Because the cryostation needs to reach cryogenic temperatures in order to fully pump the pressure down to high vacuum, this amount of time must be given no matter what temperature

data is to be taken at (besides room temperature). In addition to temperature, built into the cryostat itself we have the ability to control both sample position and a transverse magnetic field. Positional control is made possible by a stack of three piezoelectric stages that the sample is mounted to. The mass of these stages is largely responsible for the long period of time it takes for the cryostat to cool down, since they must reach a similar temperature to the sample mount. The magnetic field is supplied by a built in electromagnet with removable poles that extend into the sample chamber and supply the field between them. The temperature, vacuum, and magnetic field are controlled by a laptop connected to the cryostation, while the piezos have an additional controller on top of the vacuum pump.

4.5 Piezoelectric stages

Each of the three piezoelectric stages in the vacuum chamber controls one dimension of movement, so we have full 3D control of the sample's position in the cryostat (within reason). The piezoelectric stages in the cryostation are called stepping stages. The individual steps that these stages take can be estimated as periods of a sawtooth wave. The electric field supplied to the piezos ramps up continuously to a set voltage, causing it to expand (contract?). The mechanical portion then clamps the stage in place while the voltage quickly drops back to zero, leaving the stage in the new position. It is possible to control the voltage as well as the frequency of the wave form, affecting the distance moved in a single step and the speed at which it moves. Because of the temperature sensitivity of the piezos, care should be taken that they are always grounded before changing the temperature of the cryostat to prevent a large buildup of charge/electric field that may damage the stages. All three stages have multiple millimeters of motion available to them, but none are limited by the stage's range of motion itself. They are instead limited by collision with other parts of the vacuum chamber of the cryostat. If any of the

three stages is near the edge of its range of motion, especially if actually pushing against another part of the cryostat, all three stages will behave poorly due to the addition forces at work from the contact. If the stages begin moving the sample in unexpected ways this is the most likely culprit, and indeed the only one I have happened across.

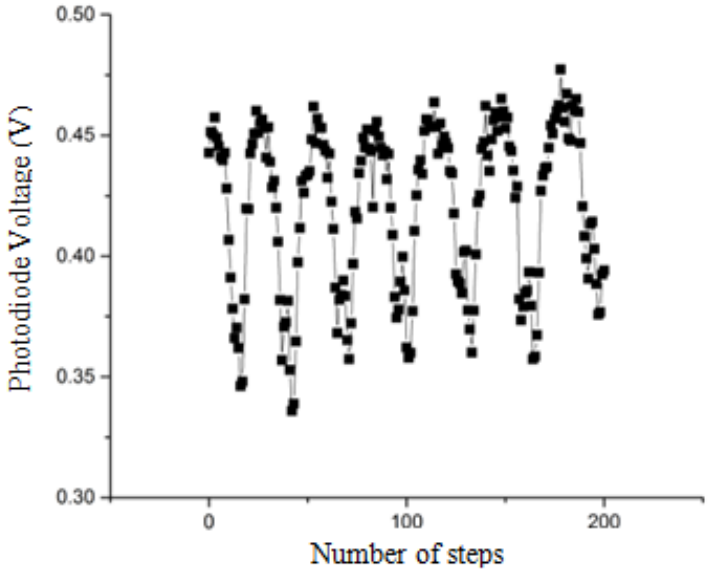

Figure 4.4 Piezo calibration
A representative scan taken when calibrating the piezo stepping stages. These measurements were taken at room temperature by collecting all laser light reflected from the sample on a photodiode. Data exhibits a large amount of noise due to subpar laser conditions present in the lab for multiple months around this time. More precise measurements were difficult to perform previous to this being fixed, but the calibration was independent of this type of noise and so was able to be performed at this point in time.

Due to the inherent noisiness of the piezo stepping stages, care was taken when calibrating the scans which use the stages to perform spatial measurements. The distance moved is not linear with voltage and even at a given voltage may be different for motion in the positive or negative direction. These stages are repeatable to within ten percent, however this changes with voltage. The sample used for calibration of the piezo stages was identical to that used for the steering mirror calibration described earlier. The sample has a grid which repeats every 10

um with 8 um squares and 2 um channels between. The calibration scans consist of reflectivity measurements being taken between every step of the piezo stage. The pulsed laser was reflected off the calibration sample and fully collected immediately after by a photodiode whose voltage was measured. Any decrease in reflectivity is therefore due purely to scattering off the edges of the channels. The laser spot is small enough that a peak was once again witnessed in signal at the center of the channels. This peak was used to measure the distance the piezo would travel each, with the peaks being a known 10 um apart. The piezo stages would travel over 50 um with each scan. The first few steps after a stage changes direction are not consistent, so the first channel peak was ignored due to the backlash present in the system's motion.

These calibration measurements were repeated multiple times at each set of experimental parameters, over a range of voltages and sample temperatures. Marisa Romanelli assisted in performing these measurements as well as creating the resulting LabView instruments. This is necessary, since the piezo stages are both voltage and temperature dependent. After experimenting with a wide range of voltages, the most repeatable measurements were found to be at 60V where the stages move approx. 1 um per step. The piezos can of course be calibrated then used to scan at any voltage desired, but Labview VI's have only been implemented to make use of this most repeatable set of parameters, with temperatures, voltages, and step sizes saved to multidimensional arrays. Scans performed at other voltages or temperature will not be as repeatable and as such may cause difficulty in determining precise spatial dependence of sample characteristics. Position scans of the piezoelectric stages should generally be performed with these known values to ensure the best possible data.

4.6 Electromagnet

The electromagnet included in the cryostation can reach sustained fields of over 600 mT at the position of the sample. The pole tips are designed to provide a uniform field in a small area between them that rapidly falls off outside of that area. The electromagnet itself has a small hysteresis that will be explained below. There are two methods of controlling the magnet. The laptop connected to the system can control the magnetic field or a BNC cable can be connected to the front of the electromagnet controller with a supplied voltage. The built-in magnet control uses a calibration run with a magnetic field probe supplied with the cryostat that attaches to the top of the sample chamber. This is a very useful method of setting the magnet to a given field quickly and easily, however the slight hysteresis of the magnet and imperfect calibration can cause the actual field to differ from the desired field by up to 5 mT. In many cases a precise field is not needed and this is acceptable. However, in cases where a precise field is needed or a magnetic field scan is being performed, it is necessary to control the magnetic field via the BNC connection on the controller. This input can be adjusted to account for the hysteresis and supply a much more precise magnetic field to the sample.

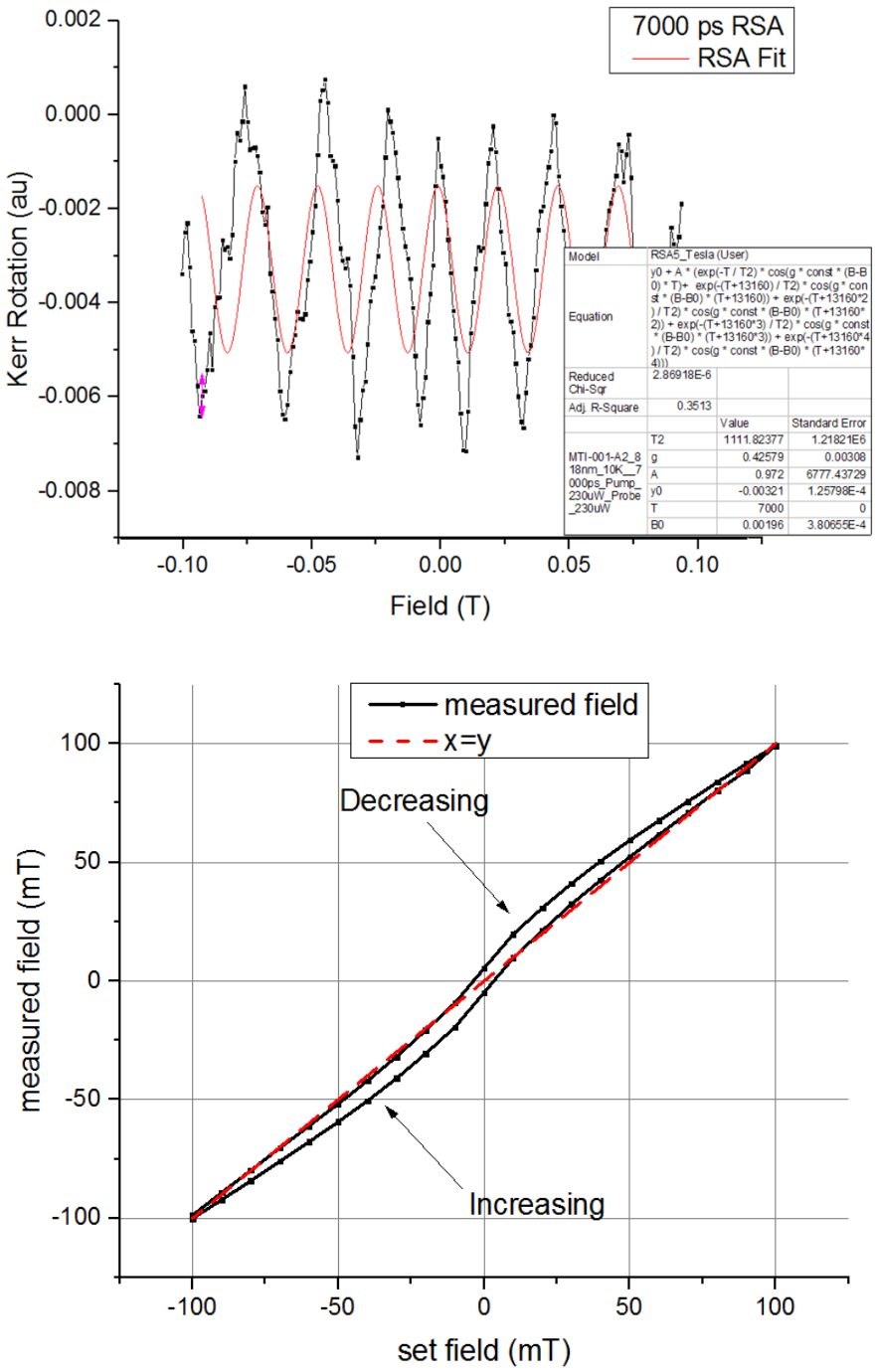

Figure 4.5 Sample RSA scan and magnet hysteresis
The top panel shows an RSA scan previous to magnet calibration. Attempts at fitting the data failed due to the inconsistent spacing of the peaks. The bottom panel shows the measured hysteresis taken after discovering its existence due to the odd signal above.

The inaccuracies of the supplied electromagnet control software were first discovered when performing test measurements of a known sample in the cryostat. The sample being studied is bulk GaAs with a previously measured spin lifetime of 30 ns at 10 K, the same temperature that was being used. The measurement performed was resonant spin amplification (RSA) [28] where the magnetic field is scanned at a set time delay and Kerr rotation measurements are performed. When the spin lifetime is comparable to the laser repetition rate (in our case 30 ns lifetime with a repetition rate of 13 ns), the spins will build up to a large value when they are being pumped resonantly. That is, the external magnetic field causes the spins to precess and if the pump laser comes in when the spins have precessed some multiple of two pi, there is constructive interference. With any other magnetic field, destructive interference occurs so with these known time scales an RSA scan of the sample should contain evenly spaced peaks, with a width that decreases with an increasing spin lifetime. However what was observed were inconsistent, irregularly spaced peaks.

Inserting a gaussmeter between magnet poles and measuring the field shows an evident hysteresis as shown in Fig. 4.5. Now that we know our magnet exhibits this, it is necessary to understand how it functions in order to take precise magnetic field scans. Often the applied magnetic field is not needed to be incredibly accurate, just near 100/200/300 mT, but for scans such as RSA the magnetic field must be accurate to within less than 1 mT or the data will be too irregular to fit with the applicable functions and extract the necessary parameters.

With this in mind, the repeatability of the magnet was tested over multiple iterations. Shantam Ravan assisted in performing these measurements as well as creating the resulting LabView instruments. The magnet was controlled via the voltage in BNC connection and set to sweep between magnetic field values that were commonly used in previous measurements, such

as from -100 mT to +100 mT. It was found that after the first scan (which initially arrives at the start from some unknown field) the second and onward scans had strong repeatability, with magnetic field points varying by < 0.1 mT. Thus, by creating known scan parameters and saving the magnetic fields to lookup tables, we were able to assemble a small selection of known magnetic field scans to use in the future. It is now possible using these methods to scan between +/- 50, 100, 150, 200, 250, and 300 mT with high precision if such measurements are needed at a future date.

4.7 Sample mounting and wiring

There are two sample chambers provided with the cryostation, one with the electromagnet and one without. The setup is constructed in such a way that the objective as well as the 4-f cage can be moved out of the way so that the sample chamber can be lifted off of the base of the cryostat/sample mount. This gives ease of access when moving samples/sample mounts into and out of the cryostat. Multiple sample mounts exist for the cryostation, allowing for multiple samples/devices to be mounted and wired at a time. These can then be switched between fairly easily with the sample chamber removed from the base. The pump/probe and other beams from the setup approaching the chamber from above means that our samples are mounted horizontally, and this grants some leeway in attaching samples to the mounts. Gravity is working for us, keeping the sample mounted and not attempting to remove it from the mount, so uncontacted/unwired samples can be attached to mounts using thermal grease (N-grease). When connected firmly, this allows the sample to be moved around and removed from the sample mount easily, without any movement when in the cryostation and provides good thermal conductivity for the sample to reach the desired temperature. When wiring is necessary, silver

paint is the preferred compound for mounting. This holds the sample in thermal/electrical contact with the mount as well as preventing any movement of the sample when wiring.

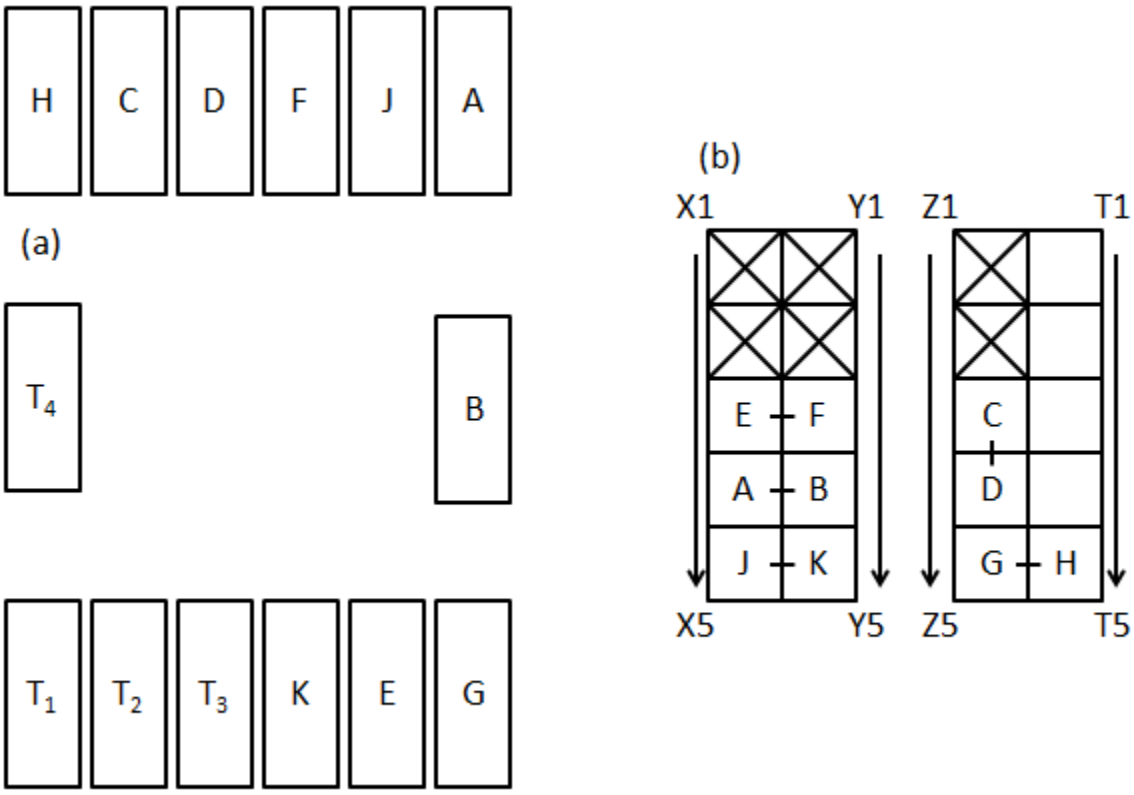

Figure 4.6 Pin-out diagrams
Current pin-out diagrams of (a) the printed circuit board within the cryostat when connected to a 10 pin breakout box and (b) the connections of that wiring to the outside of the cryostation. These may be subject to change if the 10 pin connector wires are disconnected, as the pairs of letters in (b) are connected, but the wiring otherwise exists in 5 separate pairs. Crossed out boxes are pre-wired to control the piezoelectric stages. Similar pin-outs can be determined in the future by using an ohmmeter to determine connections.

When contacted samples are mounted, a printed circuit board is attached to the sample mount that can be wired to the sample, either via wire bonding or indium blobbing. These PCBs have a 14-pin connector that leads from the sample chamber to the outside of the cryostat. The

outer pins are wired to a 10-pin connector that can be attached to any 10-pin out box. The pin-out diagrams for both the PCB and the outside of the cryostation are shown in Fig. 4.6. These connections currently allow for control of up to 10 voltages on a sample (a 10-pin connector was used instead of 14-pin as our lab was in possession of 10-pin out boxes).

4.8 Cryostat Troubleshooting

As could be imagined, a cryostation with this many different mechanisms leaves many places for something to go wrong. As opposed to helium flow cryostats, this cryostation has three mechanical pumps used for preparing the sample for study: a vacuum pump to reduce the pressure in the sample chamber to low vacuum, a cryo pump to reduce the pressure below what the mechanical pump is capable of, and a helium compressor to help it reach the cryogenic temperatures. These three pieces each have the capability of introducing mechanical vibrations to the optical table. In the past this has occurred, leading to an additional lab time dependent frequency showing up in the Kerr rotation data. The small, fast oscillation of the data was caused by a very small mechanical vibration introduced to the optical table which in turn caused the microscope objective to vibrate. When mechanical vibrations are introduced to the table, the set of translation/rotations stages and steel rods holding the microscope objective turn into an effective lever arm and amplify the movement experienced by the objective. Given the microscopic nature of the measurements performed, any motion at all has a significant effect on the signal being gathered from the light reflected off of samples.

The vacuum pump and the helium compressor run the lowest risk of causing these vibrations, as they are both contained in their controllers resting on the floor. The vacuum pump is connected to the cryostat via a pair of plastic tubes and thus is very unlikely to be the source of possible vibrations. The helium compressor, while also resting on the floor, must transport

liquid/pressurized gaseous helium to and from the cryostation. To accomplish this, it uses vacuum insulated metal tubing. This makes it more likely to transfer vibrations, but the tubes are designed to damp mechanical vibrations, so as long as the tubing is prevented from contact with the optical table itself there is negligible risk of this being the cause of the optical table vibrations.

The cryo pump is housed inside the body of the cryostation itself, making it the most likely cause of these extra oscillations superimposed on our signal. After some back and forth with Montana Instruments, we diagnosed the issue as the supporting springs on the cryo pump settling as time passed. This caused the cross bar which brings helium from the main body of the cryostat to the sample chamber to come into contact with its housing. This touch transferred mechanical vibrations from the cryo pump to the base plate of the cryostat which is secured to the optical table. Taking off the rear guard of the cryostat grants access to two bolts at the ends of the suspension springs. These were tightened to increase the support that the springs give the pump, lifting the cross bar up to the center of its housing. As the cryostation settles into place in the future, this procedure may need to be repeated to keep the crossbar from reintroducing these vibrations.

Lastly, a few notes in regards to the cryostat's ability to maintain a high vacuum environment. As stated earlier, a vacuum pump situated on the floor quickly pumps the sample chamber to low pressure, followed by a cryo pump that kicks in at low temperatures and pressures to achieve high vacuum. A good seal is necessary to achieve and subsequently maintain this high vacuum for hours of data gathering without any sort of leakage of air into the system. The sample chamber having a removable lid as well as being removable from the cryostat itself means that there are two o-rings responsible for holding this seal. These o-rings are

on the top and bottom of the removable sample chamber and are held in place by small grooves and the vacuum grease (L-grease) that helps to keep the seal. Because chamber can be opened fairly often when data is being taken on numerous samples, these o-rings are exposed to air and dust regularly. If the cryostat takes longer than five minutes to switch over to cryo pumping or signal on a sample decreases over the course of a day, this may be a sign that the o-rings need cleaning and a re-application of vacuum grease. Often times the decrease of signal over the course of a day is indicative of a thin layer of frost forming on the sample. Monolayers are very sensitive to this change in environment due to only being a few atoms thick themselves, so any small leakage of air into the system can be harmful to continued measurements. For cleaning off the o-rings, a clean room wipe is sufficient to remove the old grease/dust without risking any scratching of the ring that would damage the vacuum. Reapplication can be done with latex gloves by getting one or two grain of rice sized amounts of grease on a finger and spreading it over the surface of the o-ring to ensure complete coverage. As a final note, when the sample chamber is placed onto the cryostat base there are no moving parts used to fasten it down or to hold it in place. The pumping down of the inside pressure is the only mechanism for keeping the sample chamber in the correct position, and using any sort of clamps on the optical table to hold it in place can prevent a good seal from forming on the bottom o-ring, preventing the cryostation from reaching high vacuum.

Chapter 5

WSe_2 Device Fabrication

5.1 Introduction

Another large portion of my time at the University of Michigan was spent attempting to create workable sample devices in the Lurie Nanofabrication Facility. We are interested in applying lateral electric fields to monolayer TMDs in order to measure the mobility of optically-generated spin valley polarization, as this can help to distinguish between different proposed mechanisms for the observed spin valley lifetime, which could be due to resident spin-polarized electrons or changes in excitonic density [17,22]. In addition, the spin drift length is an important parameter for spintronics applications. Many iterations were gone through utilizing the first direct write lithography techniques that our group used to our final devices with mysteriously disappearing signal. There were many difficulties in creating these devices, from aligning contacts across 10 um samples with very low contrast against the substrate to needing to learn wire bonding to wire with these new, smaller than previously used contacts. Through trial and error, a solid foundation has been laid for future work in contacting these sorts of MOCVD-grown TMDs, and indeed the direct write techniques described here have already been put to further use by other graduate students in the Sih lab group.

5.2 Direct Write Lithography

When performing measurements on semiconductor devices that need the presence of an electric field, metal contacts are often deposited onto the semiconductor surfaces, due to the much smaller resistivity of metals. To do this, samples are placed into an electron beam evaporator. E-beam evaporators use beams of electrons directed at metal sources held in a crucible to heat the metals up enough that they evaporate. This gaseous metal then diffuses through a vacuum and is deposited on all surfaces with direct line of sight to the area where it is being vaporized. Because the metal is deposited on every exposed surface, it is necessary to in some way define where we want the metal to end up on the sample and prevent the metal from being deposited at all other positions. This can be done by covering the entire sample in a photoresist followed by exposing specific areas of the photoresist-covered sample to blue light. Photoresist is a light-sensitive material that undergoes a chemical change when exposed to certain wavelengths of light. In our experiments, positive photoresist was used, which degrades when exposed to blue (or higher energy) light. Thus, when a developer is introduced to the surface, it will only dissolve away the areas that were exposed. Negative photoresist can also be used, which is strengthened by the exposure and therefore only the exposed areas remain on the sample when the developer is used.

Typically, the areas on a sample which are to be exposed to light are defined by using a mask placed directly over top the sample. This mask is a glass square mostly covered in a light-absorbing metal. This mask has previously undergone its own lithography process to remove a certain pattern of the metal on it, leaving those areas transparent. The mask is then held in place above a sample and the entire area is exposed to blue light, with only the transparent areas of the mask allowing the light through to affect the photoresist-covered sample. In this way, many

identical sets of contacts can be deposited onto a variety of different samples to allow for similar measurements to be made across differently grown semiconductor samples.

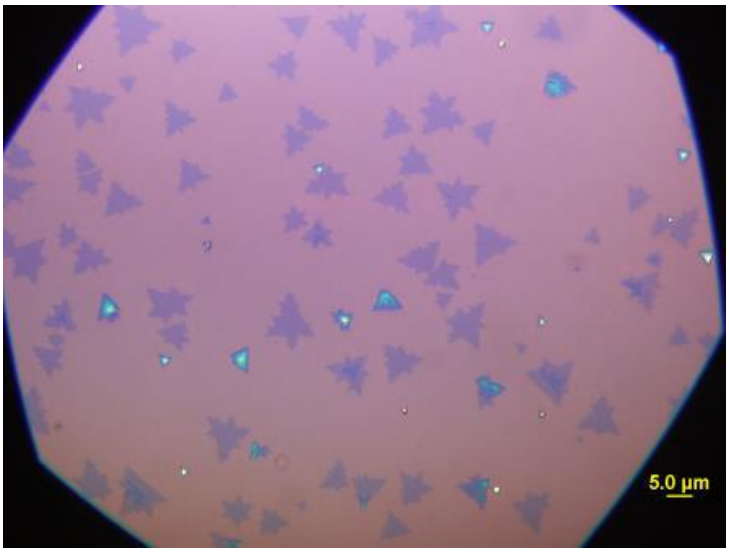

Figure 5.1 First samples used for device fabrication
Optical microscope picture of the first samples used, light pink is the substrate while the slightly darker color is monolayers. Brighter blue spots are thicker (bilayer or more) growth areas.

Our case is different as, instead of exposing homogeneously grown wafers with a mask, we must align contacts across WSe2 flakes of differing size and shape. The WSe2 samples used here were grown by metalorganic chemical vapor deposition (MOCVD) on a silicon/300 nm silicon dioxide substrate by the Jiwoong Park group at the University of Chicago. These samples have triangular and six-sided star-shaped grains around 5-15 um across, an example of which can be seen in Fig. 5.1. Because the material we are studying is a monolayer, it has very little difference in optical contrast compared to bare substrate, and thus it is impossible to identify individual flakes when viewing the sample through photoresist. Therefore, due to the inhomogeneous and sparse nature of these flakes, creating a pattern for contacts on a mask and placing the mask over a photoresist-covered sample to determine contact placement is unlikely to

create a pair of metal contacts across an individual flake. So, we must utilize a different method of contact alignment to guarantee that our contacts end up aligned with WSe2 flakes. All the methods described here were performed using equipment in the Lurie Nanofabrication Facility with initial assistance from mentors there, with special thanks to Vishva Ray. The method used for creating our samples is called direct writing, or maskless lithography. In this, instead of creating a mask and exposing the entire mask, the machine originally used to create the pattern on the mask is instead used directly on the sample itself. This machine, the Heidelberg Mask Maker, shines an LED focused down to a < 100 nm spot size on our sample with high precision following a pattern supplied to it. Using this method, we only expose the areas of the photoresist-covered sample that we wish to deposit contacts on, this time by directing the light itself instead of by blocking it with a mask.

5.3 Aligning Contacts with Flakes

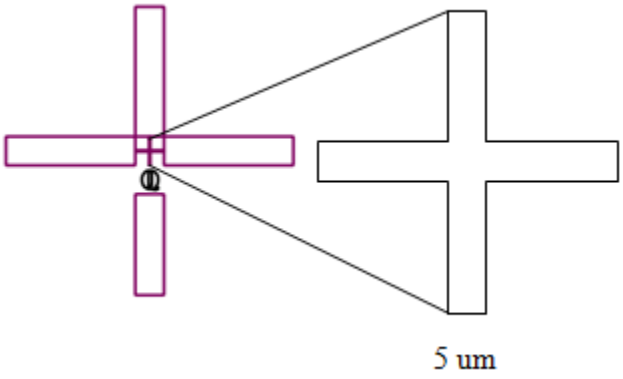

Figure 5.2 Alignment marks
Blown up image of alignment marks used to position the first pairs of contacts deposited on the sample. The smallest measurement of the plus is 5 microns. Measurements were taken from an inside corner of the small plus to ideally provide sub-micron precision.

While the direct-write method allows for contacts to be deposited at any position and orientation desired on a sample, it alone does not solve the problem of aligning these contacts across flakes within a 1-2 micron allowance, as we can still not see the flakes through the photoresist. First, alignment marks must be placed on the sample that can be seen through photoresist. The flakes that we wish to be contacted can then be located with respect to the alignment markings, and then the contacts can also be placed using those same marks. The first sample used to experiment with this method of contact deposition was named WSe254#3; this growth cycle produced WSe2 flakes that were around 8 um across. Alignment marks are placed at two opposing corners of the 1 cm x 1 cm sample. The alignment marks use the same method of direct-write exposure and deposition as we use for the contacts themselves. The marks, an example of which is seen in Fig. 5.2, have two cross-shaped sections and a letter to keep them distinguishable. The large cross is large enough to easily be seen by eye, while the smaller cross has a minimum dimension of 5 um, allowing its corners to be used for a precise measure of location/alignment. With the alignment markings placed, a scanning microscope is then used to determine the relative positions of larger flakes that we wish to deposit contacts across. Because the cryostat cold finger can only fit samples that are around 5 mm x 5 mm, four flakes were found near the centers of each quadrant of the original chip. Because this was the first attempt using these methods for making devices and we were unsure of how precisely we could perform the alignment using the scanning optical microscope, the contacts were designed with a 3 um gap between each pair to ensure a couple micron leeway in alignment. In this way, four potential devices are made in the lithography process.

Using the direct write method, the four sets of contacts are then deposited. The entirety of the lithography process involves first spinning photoresist onto the sample, then using direct

write to expose the sample. The photoresist is then developed to be removed from the areas where contacts are desired. Next, the e-beam evaporator was used to deposit 100 nm of gold to act as the contacts, followed by a liftoff procedure in which the sample was soaked in acetone in order to dissolve the remaining photoresist and remove the metal deposited on the resist. After liftoff, only the metal deposited directly onto the sample remains. Inspection with an optical microscope revealed that ~1 um fringes of gold remain at the edges of the contacts, as seen in Fig. 5.3(a). Given that the spacing of the contacts is only 3 um, these fringes cover a substantial area of the flake that optical measurements need to be performed on. The devices were then sonicated in an attempt to clean up the contact edges. As seen in Fig. 5.3(b), this did succeed in removing the fringes from the edges of the contacts. However, sonication revealed two problems with the contact deposition. First, the sonication removed not only the fringes but also parts of some of the contacts, destroying two of the devices. Second, the contacts did not end up aligned with any flakes at all. Both of these problems need to be remedied before useful devices can be realized. To avoid contacts being destroyed via sonication or other physical processes, better adhesion between the contact and sample/substrate is necessary. In addition, for better positioning of contacts across flakes, an improved method of alignment is needed.

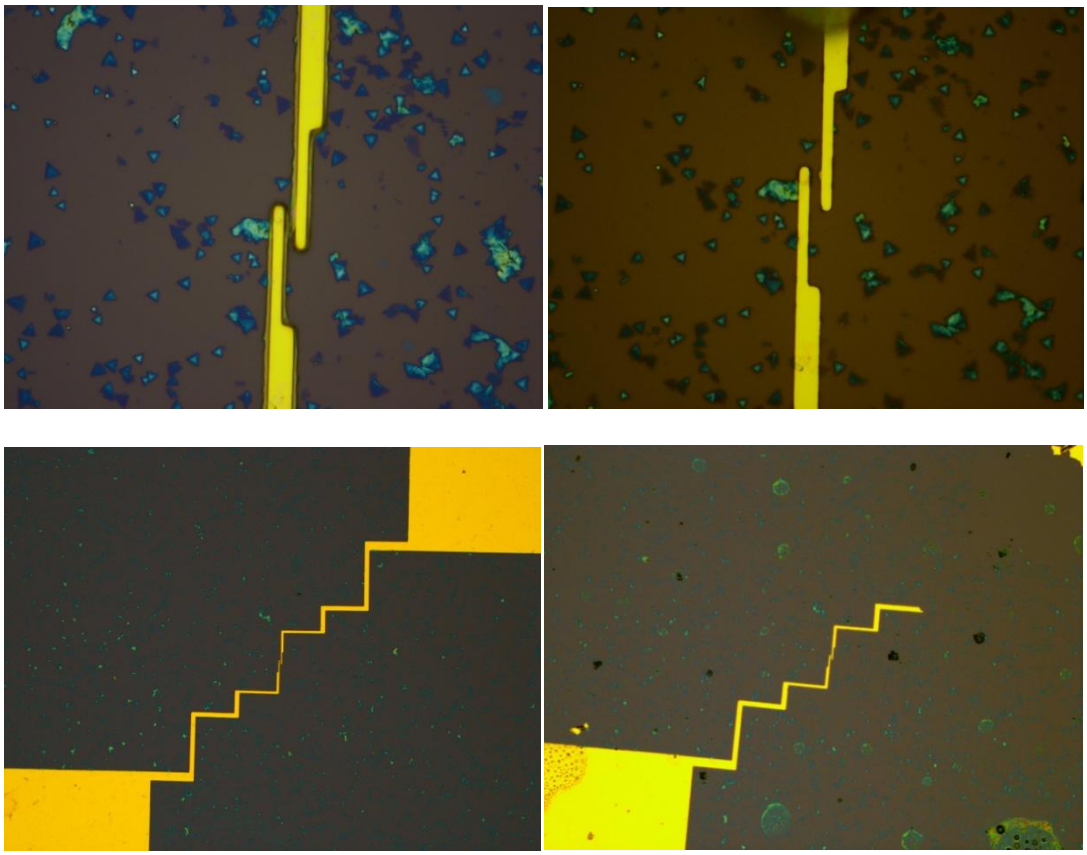

Figure 5.3 Contacts on samples, sonication
Left side: sample after liftoff but pre-sonication. Fuzzy edges are seen on the contacts which must be removed if we wish to study the sample between the two contacts using optical techniques. Right side: post-sonication. Edges were removed very well, however there is no monolayer visible between the two contacts, meaning that the alignment procedure was flawed. In addition, for some of the contact pairs large portions of the contacts themselves were destroyed by the sonication procedure.

To solve the first problem of contact destruction, a 5 nm layer of Titanium was added to the metal deposition in order to strengthen the adhesion of the contacts to the sample. The thin layer of Ti has negligible effect on the electrical properties of the system, while both strongly bonding to the SiO2 substrate and alloying with the gold contacts. The second problem requires a change in the alignment markings' structure and spacing. A new layout of alignment markings is created, with dimensions comparable to the smaller cross used in the original layout. In addition,

instead of placing them at opposing sides of a 1 cm square, they are situated approx. 25 um apart - near enough to both be seen within the frame of a 100x microscope objective. A single photo can then be used to locate the flake which we desire to contact and study, and purely geometrical methods can provide the position and angle at which the contacts should be deposited with respect to the alignment markings.

5.4 Wire Bonding

Another challenge that must be overcome when working with these small samples is wiring between the mounted samples and the printed circuit board attached to the mount itself. Previously in the lab, indium blobbing was the method of choice for wiring between samples and cryostats. Using this method, mechanical pressure is applied by hand to simply push and stick small indium blobs onto contacts and PCB pads along with wires. This method still has its use when wiring only two contacts to the PCB, however some of our device designs have four contacts, meaning that indium blobbing by hand is not precise enough to ensure the four contacts do not have any shorts between them arising from the blobs. Thus we made our first foray into learning to wire bond.

Wire bonding is a method often used to connect semiconductor devices with their surroundings. A small, in our case .0007 inch diameter, gold wire is first clamped in a wedge which resembles a sewing machine needle. The wire is then brought into contact with the metal contacts on our device, and is then bonded to the sample by applying pressure and ultrasonic vibrations to the connection. These forces cause the gold wire and metal it is in contact with to briefly liquefy before solidifying and becoming a single solid crystal. The wedge is then lifted off the device and moved laterally to be above where the second connection will occur. The wedge is once again lowered, this time to the PCB pad, where another ultrasonic bond is formed.

The wire is then broken at the location of the bond while it is still clamped to the pad, removing all excess wire. When using a wire bonder to wire devices, there are multiple variables in play. For both ultrasonic bonds, the force applied, power supplied via ultrasonic energy, and the time over which these are applied are all controllable. Depending on the composition of the metal which is being bonded to and the type of wire used, reasonable starting points for these variables have been found. However, it can be difficult to tease out which variable should be adjusted when having trouble making wire bonds. If the force or power is too low, the bond is unlikely to stick, but if either is too high the wire has a high likelihood of breaking at the point of the bond. In addition to the bond initially forming, it also has to survive the wire being raised and dragged over to the second bond site. In the end, adjusting all of these parameters for both bonds ends up being more of an art than a science.

When first attempts were made with our samples, the contact thicknesses used for deposition were found to be on the low side for usage in wire bonding. As a result, a very precise balance had to be struck between causing a bond to stick and liquefying the surface of the gold contact where the bond was occurring so much that it was lifted off along with the wire when attempting to make the second bond. Many adjustments of bonding parameters occurred with each resulting in a very small portion of the sample contact being destroyed (the wire is < 20 um in diameter after all). After bonding parameters had been found over the course of a few days in the clean room, subsequent wire bonding efforts found much faster and easier success, with nicer looking sample surfaces afterwards. Increasing the contact thickness from 100 nm of gold to 200 nm of gold (both including the 5 nm titanium adhesion layer) also allows for a larger range of usable parameters, further increasing the ease of wire bonding.

Figure 5.4 Initial wire bonding results
The many iterations of force, timing, and power left contact pads resembling porcupines prior to creating working wire bonds. The right picture shows the arch of the bonded wire over the edge of the sample down to the PCB, demonstrating the ability to wire between different heights without the wire contacting the edge of the sample.

5.5 Electrical and Kerr rotation measurements on processed devices

At the same time these changes were being implemented in the device preparation process, we received a new set of samples with a different surface geometry. Instead of many individual flakes being present on the sample, the growth conditions had created a large, mostly monolayer area with very few bilayers. This sample provided a large continuous film of monolayer WSe2, meaning that we would not need to use alignment markings to place contacts. To begin with, the sample was placed in the cryostat to ensure that Kerr rotation could be seen on a sample grown like this. Contacts were then deposited in a cross pattern, with the closer pair being 10 um across and the further pair 20 um. Two pairs were created instead of the usual one because the continuous film allowed them to be placed further apart while still allowing a path for current to flow. The ten micron pair would ideally be used for measurements as this would be

comparable to the spacing we could place across large individual flakes, allowing comparison of continuous and single flake measurements. The twenty micron pair existed simply as a back-up to the first pair that was far enough away that it would not affect current flow when the close pair was used for measurements. Device preparation proceeded smoothly, and soon we had a set of contacts as seen in Figure 5.6(b)-(c). Note that the small grain size (100s of nm) renders the individual grains impossible to distinguish with our optical microscope.

In order to determine whether the contacts were working, electrical measurements were performed by applying voltages and measuring current between the source and drain contacts while varying the back gate voltage (Fig. 5.5(a)). The substrate used for the growth of these samples was Si with 300 nm SiO2 thermal oxide on the top surface. The back of the substrate was slightly scraped off and silver paint was used to adhere to the cold finger. Therefore we were able to apply the back gate voltage between contacts on the face of the sample and the cold finger itself, providing an electric field across the dielectric SiO_2. These measurements found that there was an 8 pA current between the source and drain contacts when a source-drain voltage of 0.1 V and a back gate voltage of 20 V was applied, as seen in Fig. 5.5(b). In general, the back gate should create an electric field in the dielectric substrate causing an initial flow of charge carriers to/from the sample material. This current should however quickly decrease to essentially zero as the carrier concentration in the sample reaches a steady state. With a positive source-drain voltage applied, we should then see a positive current with some dependence on the back gate voltage caused by the change in carrier concentration. However, the sign of the source-drain current changed with the polarity of the back gate voltage, indicating some additional

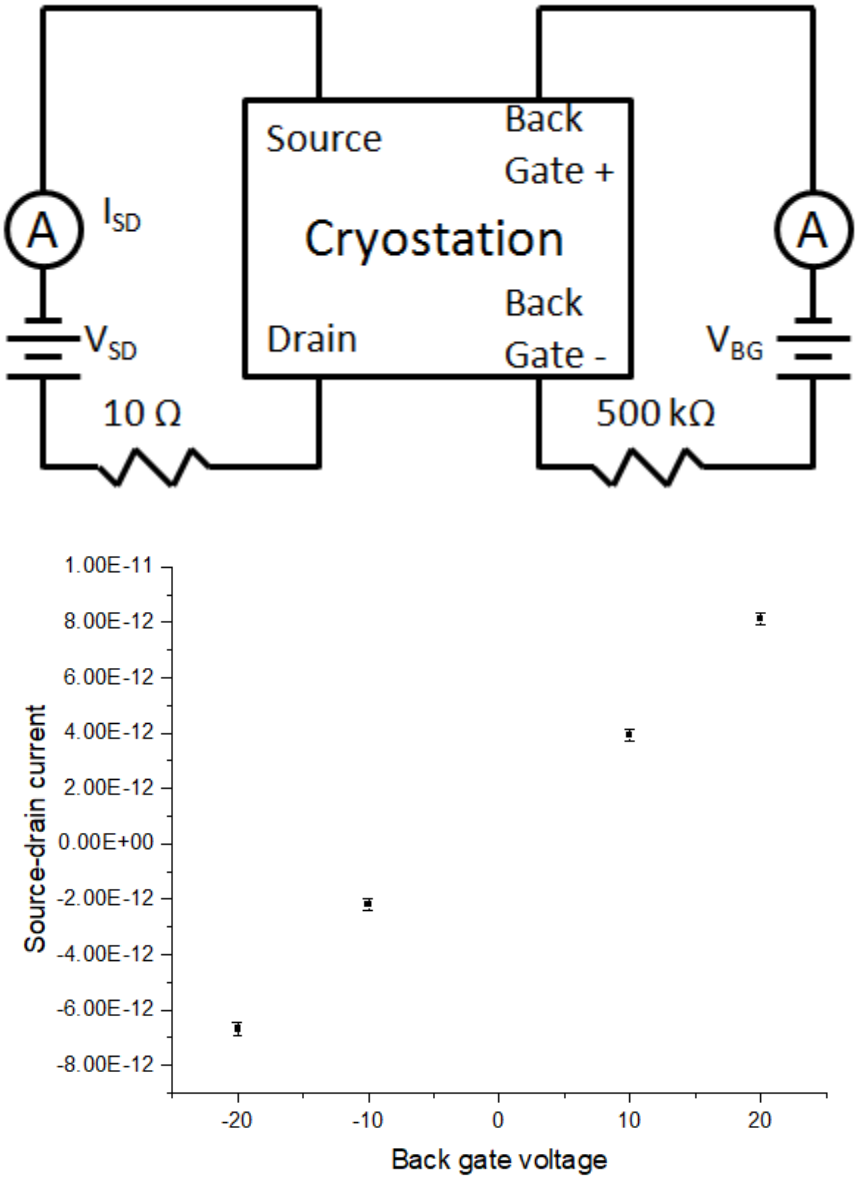

Figure 5.5 Electrical measurements
(a) Wiring diagram of back-gated sample. One back gate terminal was connected to the substrate of the sample via electrical connection to the cold finger itself, while the other was connected to a contact deposited on the sample (multiple were experimented with, all with the same results)
(b) Source-drain current vs. back gate voltage on this sample. Measurements were taken at room temperature and pressure. Note the nearly linear dependence of current on back gate voltage.

current being driven by the back gate voltage. In an attempt to narrow down the explicit source of this current, measurements were repeated with the back gate voltage connected to various contacts on the sample, including a contact that was not used as the source or the drain in this circuit. All measurements showed the same result, but this nevertheless provides proof that there is an electrical connection between the source and drain contacts. Performing spin drag experiments, where a source-drain voltage is supplied and Kerr rotation measurements are taken as a function of time and position to track the spin packet, should allow us to view more accurately what is occurring in the sample in the future.

Kerr rotation measurements were then taken with the pump and probe beams located between the sets of contacts. However, the Kerr rotation signal is now significantly decreased from the original measurements performed on the same sample (Fig 5.6(d)-(e)). To assure that this is not caused by some sort of reflection/interaction of the laser beams and the contacts, the same measurements are repeated in the same general area, but far enough away that the contacts could not have any effect on the optical measurements. This unfortunately showed the same result; signal on the entire sample is significantly harder to obtain and decreased in amplitude from previous measurements.

Monolayer TMDs are known to degrade over time, even when stored in nitrogen or vacuum environments. Given that device preparation procedures were in the process of being developed when these samples were obtained and wire bonding was first learned/performed on these devices, it was possible that the approximately one month spent going in and out of the clean room for device creation and wiring had caused the sample to degrade to a point that it was no longer possible to receive clean optical signal from it. We thus needed a new set of samples to apply what we'd learned to, and pattern/contact in a shorter period of time.

Eventually, we acquired a new growth of WSe2 with two distinct areas of growth. The outer edges of the chip contained individual large, 12 um flakes well suited for the processes devised earlier. On the inner area, increased flow had caused a denser pattern where flakes had somewhat grown into each other. Initial measurements were immediately taken on individual flakes to provide a baseline for signal amplitude/lifetime that we could expect from this growth going forward. The new design of alignment markings was deposited, and contacts were successfully placed across individual flakes. Following this, the contacts were wired to and the device was ready for study. Under a week had passed since initial measurements were taken. Unfortunately, once again the Kerr spin valley signal had all but disappeared from the sample. To test whether the passing of time had once again caused the sample to decay, unprocessed areas of this growth cycle had been saved and were then placed in the cryostat for study. Surprisingly, signal was present and it was comparable to that which had been found immediately after the sample had been received. Therefore, another step of the device preparation process has to be responsible for the destruction of the WSe2 samples. Multiple cuts were taken from the unprocessed sample and subjected to varying amounts of the device preparation procedure. There are three major steps in the process where the sample has a large interaction with outside influence that may be responsible for this destruction: 1. The spinning of photoresist and developer onto the sample. 2. The deposition of metal onto the sample. 3. The liftoff process where the sample is soaked in acetone.

These three steps must all happen in this order for a device to be created using photolithography. This means that four data points must be taken to determine where exactly in the process the spin signal is being destroyed. Two have already been demonstrated: a sample with no work done to it and one with all steps completed. The third is a sample where photoresist

and developer are spun onto the sample and immediately rinsed off with acetone. The fourth has photoresist and developer spun onto the sample, but then is soaked in acetone emulating the liftoff process. With these last two samples prepared, we place them into the cryostat for study. We find that the sample where the photoresist/developer was removed with a quick acetone rinse has maintained its signal strength. However, the sample that had been subjected to the liftoff process had lost its signal.

We can therefore conclude that the acetone soak is the primary culprit for the loss of signal on the prepared devices, and not the passage of time that was originally suspected. Luckily the photoresist and developer themselves do not cause any destruction of the WSe2 flakes. However, removal of the photoresist and metal that is deposited on top of it requires a liftoff process of some sort. A new method for performing the liftoff or a larger change in the photolithography process is necessary to perform measurements on contacted samples of this material. We are still in possession of unprocessed MOCVD grown WSe2 samples though, and very little work has been done looking at this type of growth.

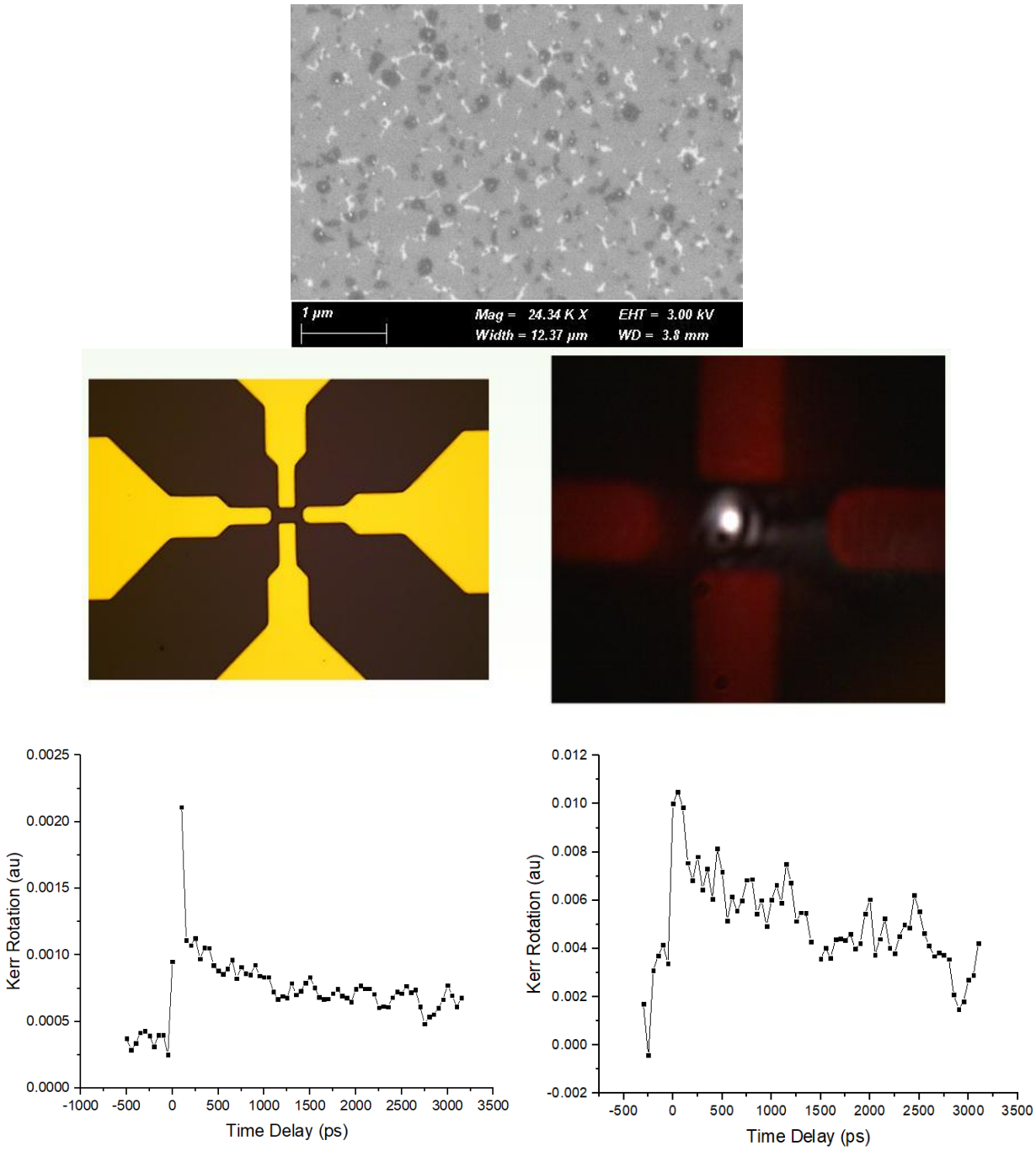

Figure 5.6 Liftoff procedure causing loss of signal
(a) Electron microscope picture of sample prior to device fabrication procedure. Grains are sub-micron size. (b), (c) pictures of contacted sample via optical microscope and once held in the cryostat, with the laser beam spot between contacts. (d) Kerr rotation measurements taken prior to fabrication This data was taken at 10 K, with 2.4 mW pump power and 0.4 mW probe power at 742.5 nm laser wavelength. (e) Kerr rotation measurements after fabrication using identical experimental parameters. Post-fabrication data was averaged over multiple scans to achieve comparable noise levels.

Chapter 6

Results and Data for MOCVD-Grown Monolayer WSe2

6.1 Introduction

In this chapter we will see what could be described as the final results of my time at Michigan. We look at how the different types of measurements that are made possible by the Kerr microscopy setup can be combined to provide a variety of information about an individual sample. Following this, there is an investigation into signal degradation in areas of samples with closely packed grains from the growth process.

6.2 Spatially-resolved Measurements of Spin Valley Polarization in MOCVD-Grown Monolayer WSe_2

The following work has been published in reference [8]. The MOCVD-grown samples were provided by Jiwoong Park's research group and grown by Fauzia Mujid.

6.2.1 Introduction

Transition metal dichalcogenide (TMD) monolayers have been the focus of intense study over the past decade. While bulk TMDs have an indirect bandgap making them less suitable for optical measurements, when these materials are thinned down to a single van der Waals layer,

the band structure transitions to a direct bandgap at the K point [10,11]. Another interesting property of TMD monolayers is that spatial inversion symmetry breaking combined with strong spin-orbit coupling leads to valley-dependent optical selection rules and an opposite spin-orbit splitting between K and K' valleys [20,29]. Thus, the manipulation of optical orientation can be used to create a spin valley polarization. These spin valley polarizations have been shown to have potentially long lifetimes, on the order of nanoseconds [13,17,18,22,26,30]. These properties, in addition to their two-dimensional nature, make TMDs attractive materials for the formation of spintronic heterostructures [31-33]. While encapsulated and/or exfoliated monolayers of these materials can have more pristine optical properties and exhibit longer spin valley lifetimes [33,34], monolayers grown via processes such as MOCVD are important to understand due to the scalability they offer compared to that of mechanical exfoliation [35].

In this chapter, we utilize time-resolved Kerr microscopy (TRKM) with micron scale spatial resolution to investigate the spatial dependence of spin valley polarization in monolayer MOCVD-grown WSe_2 and observe a non-uniform Kerr rotation amplitude. Multiple triangular flakes are examined to determine the repeatability of the observed pattern. Spatially resolved microphotoluminescence (micro PL) and reflectivity measurements are then used to investigate the origin of the nontrivial spatial pattern in the WSe_2 flakes.

Lastly, a 4-f setup is used to steer the position of the pump laser beam on the sample relative to the probe beam. This allows pump-probe spatial overlap scans to be performed at multiple time delays to determine what role, if any, diffusion plays on the time scale of the spin valley lifetime.

6.2.2 Methods

The WSe_2 monolayer flakes are grown using metalorganic chemical vapor deposition (CVD) on Si/SiO_2 substrates. As seen in Fig. 6.1(a), a typical grain has a triangular or six-sided star-shaped pattern and ranges from 5 to 10 microns across. The samples are then mounted in a closed-cycle helium cryostat. For the remainder of this paper, measurements are conducted with the sample cooled to 10 K unless noted otherwise.

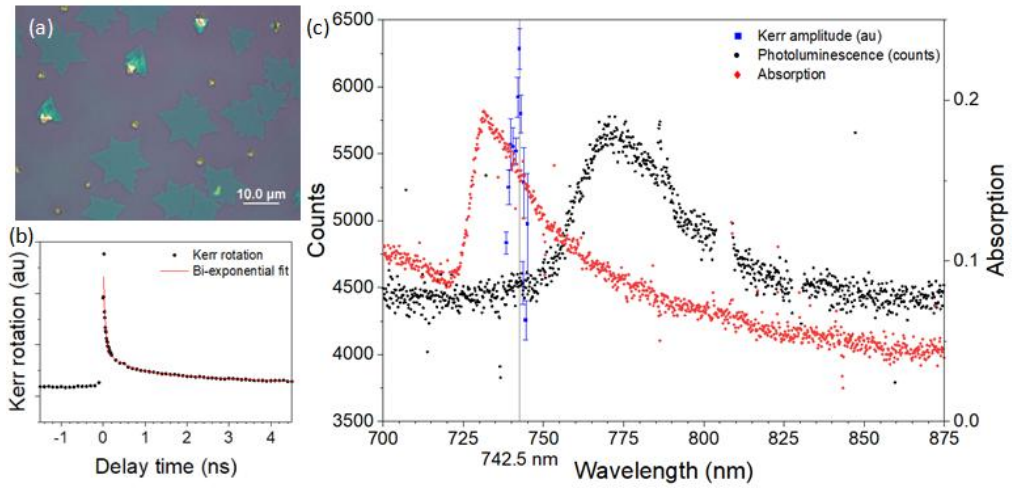

Figure 6.1 Wavelength dependence of sample
(a) Optical image of multiple flakes on the sample used in this research. (b) TRKM data (points) with fit for bi-exponential decay (solid line). Negative delay data represents a 12-13 ns delay after the previous pump pulse due to the 13.16 ns repetition rate of the laser. (c) Photoluminescence spectrum taken over 100s with the sample held at 10K (black). The pump used is a 533nm diode laser. No excitonic side-peaks are seen in this sample. Also shown is the amplitude of long-lived spin valley signal extracted from TRKM measurements as a function of the pump/probe laser wavelength (blue). Finally, a white light absorption spectrum is shown with a peak near 730 nm (red). This was calculated by taking two spectra of the white light source, one reflected from a flake and the other from the substrate. The on-flake spectrum was then subtracted from and normalized by the off-flake. Artifacts in the PL spectrum at 805 and 828 nm were removed.

The TRKM measurements are performed using a mode-locked Ti: Sapphire laser with a repetition rate of 76 MHz. This laser is split into two beams, a pump path modulated between

left- and right-circular polarization at 50 kHz by a photo-elastic modulator and a probe path modulated by an optical chopper (789 Hz). The relative time delay between the two beams is adjusted by a mechanical delay line in the pump path before they are recombined and directed through a 100x microscope objective to a ~2 μm spot on the sample (determined through spatially-resolved reflectivity measurements on a calibration sample). Valley polarization is generated by the circularly-polarized pump pulses [29,36] and measured through the Kerr rotation of the linearly-polarized probe pulses. This rotation is measured by directing the reflected beam to a photodiode bridge through a Wollaston prism, separating the horizontal and vertical components and taking their difference. The pump and probe beams are each balanced previous to measurements using half-wave plates for the most efficient lock-in detection. A representative TRKM plot with a bi-exponential fit can be seen in Fig. 6.1(b). In addition to the time delay, the position of the pump laser on the sample can be scanned relative to the probe spot, allowing pump-probe overlap scans to be performed. This, combined with changing the time delay allows us to view any changes that the shape and/or position of the created spin valley packet may undergo over time. Kerr microscopy measurements are initially taken at a range of wavelengths to determine the optimal wavelength for continued study (Fig. 6.1(c)) and temperature-dependent measurements show a substantial decrease in lifetime as temperature rises, in agreement with previous studies [13,17,19,26].

In addition to the wavelength dependence of the Kerr signal, the photoluminescence spectrum and white light absorption measurements are also shown in Fig. 6.1(c). The micro PL spectrum shows a broad peak centered around 770 nm with none of the excitonic side peaks often seen in TMDs [17,19,26]. This may be caused by differences in the MOCVD growth technique which can cause the photoluminescence to be mediated by localized defects [37]. Due

to this, it should be noted that the PL and TRKM peaks are offset by 60 meV in these samples, with the Kerr signal disappearing completely more than 15 meV (~7 nm) away from the Kerr rotation peak at 742.5 nm. In contrast to the PL spectrum, however, white light absorption measurements show a broad feature with a peak near 730 nm that the Kerr signal falls within. This absorption peak/Kerr signal is likely caused by the A exciton resonance which has been shown near these wavelengths [38].

6.2.3 Results

We report data using multiple flakes from a single WSe_2 growth. Following from Fig. 6.1(c), measurements are taken with pump and probe beams at 742.5 nm. Using stepping piezoelectric stages located within the cryostat, TRKM measurements are repeated at multiple points traveling across the first flake, Flake A, which is approx. 10 μm in diameter (Fig. 6.2(a)). The individual scans show a consistent bi-exponential decay with an initial fast decay of time constant t_1 ~100ps and a longer decay with t_2 ~3ns. Previous studies have also shown multi-exponential decays providing the best fitting for TRKR measurements on TMDs [13,17,26]. Fig. 6.1(b) shows one such scan overlaid with the best fit bi-exponential curve.

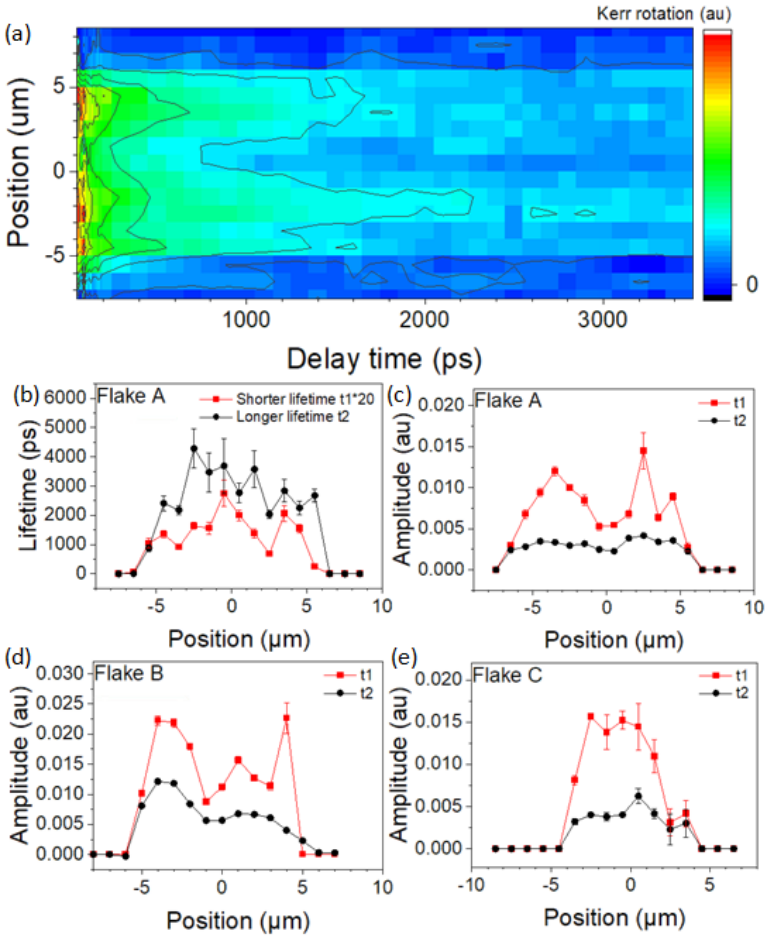

Figure 6.2 Spatial results
(a) Kerr rotation measured as a function of position across the flake and pump-probe delay time. Contour lines are included as a guide to the eye. (b) Spatial dependence of polarization lifetimes extracted from bi-exponential fits across the first 10 μm WSe_2 flake. Lifetime of shorter-lived spin signal is multiplied by a factor of 20 for comparison. (c) Spatial dependence of the amplitudes of the shorter lifetime (red) and longer lifetime (black) decays. (d), (e) Spatial dependence of the amplitudes of the shorter (red) and longer (black) lifetime decays across another flake of similar 10 μm size (d) and a smaller, 7 μm flake (e).

Looking closer at Fig. 6.2(a), we see a nontrivial spatial dependence of the TRKM signal while scanning across Flake A. The amplitude of the Kerr signal has a noticeable drop in the center of the flake at later time delays. A similar nontrivial spatial dependence has been observed in similar monolayer TMDs, WS_2 [26] and MoS_2 [38]. To further investigate this phenomenon in our samples, we plot the fitting parameters t_1 and t_2, as well as the amplitudes of the two

exponential decays, A_1 and A_2, respectively (Fig. 6.2(b-c)). Two contrasting features can be seen from this. First, there is no noticeable spatial dependence of the decay time across this flake; secondly, the amplitudes have a peak near the flake's edges and a dip near the middle. Continued measurements show this drop to be small but repeatable across this flake.

To ensure this is a consistent phenomenon and is not unique to a single flake, measurements are repeated on two additional flakes: a second flake of similar size (Flake B) and a third with a smaller width of ~7 μm (Flake C). The results of these measurements can be seen in Figs. 6.2(d) and (e), respectively. In Flake B, we once again see an amplitude drop in the center of the flake, more noticeably for the longer lifetime than the shorter lifetime decay. However, the smaller Flake C does not show this same few micron dip in its spin valley amplitudes. This is possibly due to Flake C not being large enough for the offending area to exist at its center.

There are several possible effects that could cause the nontrivial spatial variation of the Kerr signal that we observe. The effects that we will focus on here are the potential spatial inhomogeneity of the optical properties of the flake, which could change the efficiency of optical spin pumping and/or detection, and diffusion of the optically-pumped spin valley polarization. Previous studies have shown a strong spatial inhomogeneity of the PL in other TMD samples [39,40], with patterns similar to what is seen in our spatially-resolved Kerr rotation data. This would provide evidence that the flakes have stronger optical coupling on the edges than in the center. Similarly, a measurement of the reflectivity at the pump-probe wavelength could provide a simple explanation for the spatially-dependent signal strength. Lastly, spin valley polarization diffusion away from our optical spot occurring on a comparable nanosecond time scale would cause a reduction in signal and thus the fit lifetime. This would be more noticeable in the center

of the flake, since diffusion near the edges could reflect from the boundary of the flake and thus keep a greater number of spins within the area that the probe beam measures.

First, we perform spatially-resolved photoluminescence measurements to compare with the Kerr data. Once again, Flake A is stepped through the beam path to obtain spatially resolved data on individual flakes, this time using a 533 nm pump laser for PL excitation. Fig. 6.3(a) shows the integrated peak normalized by the background counts for the PL spectra across the first flake measured, and we note that all three flakes showed similar results from the photoluminescence measurements. Examining our spatial PL data next to the TRKM magnitude data shown for the same flake in Fig. 6.3(b), we see that, in contrast to the variation observed across the flake in the Kerr amplitude measurement, the PL signal reaches a maximum once the beam is fully on the flake then remain constant until moving off the flake. We note that the PL amplitude changes more gradually near the flake edges compared to the Kerr amplitude. Whereas the Kerr amplitude is measured using a pump-probe technique and depends on the spatial overlap of the pump and probe beams, photoluminescence is generated from a larger volume of the sample, based on where the excitation light is absorbed and carrier diffusion. We utilize a 50 μm pinhole between a collimated lens pair in the collection path to improve the spatial resolution. The reflectivity data in Fig. 6.3(c) also shows a similar homogeneity across the center of the flake. The reflectivity data was found by calculating the sum of the two diodes of the photodiode bridge, as compared to the difference which supplied the Kerr rotation. The PL and reflectivity data both indicate that the spatial dependence of the Kerr magnitude is not due to some change in the optical properties between the different areas of a flake.

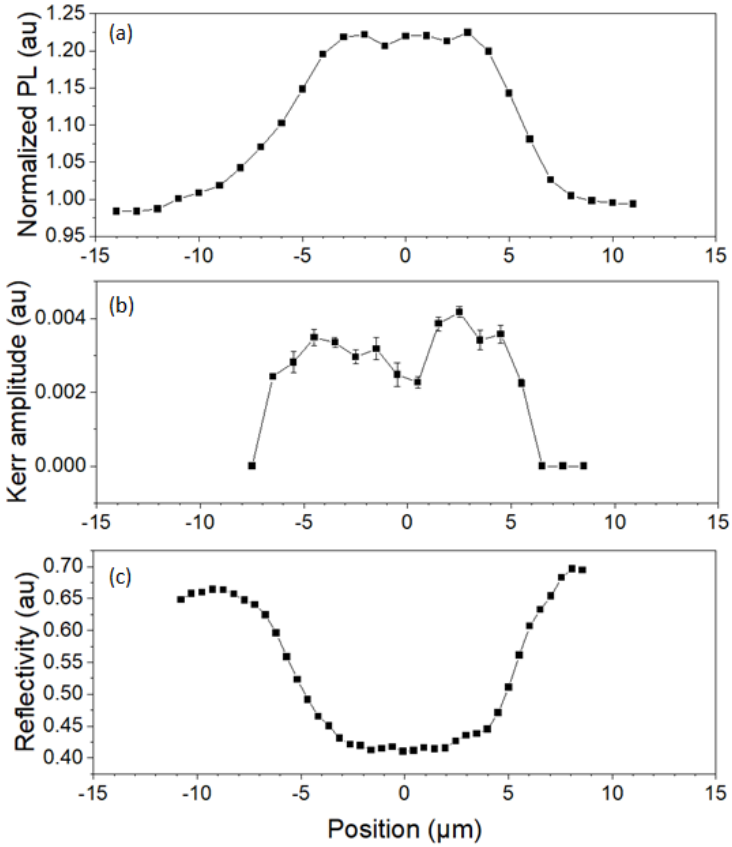

Figure 6.3 Comparison of spatial results from varied measurements
(a) Spatial dependence of the integrated intensity over the PL peak from 760 to 780 nm normalized by off-peak background signal. (b) Spatial dependence of the long-lived spin signal's amplitude across the first flake. (c) Reflectivity data taken from a piezo scan across the same flake, calculated using the total probe intensity reflected from the sample and directed to the diode bridge.

Lastly, the 4-f setup shown in Fig. 4(a) is used to perform pump-probe overlap scans to determine whether spin valley diffusion is occurring on the same time scale as the Kerr signal. This configuration utilizes a pair of planes that are four focal lengths apart where any light directed through the plane and into the first lens will exit the final plane at a position and angle reflected across the shared optical axis. By placing a motorized steering mirror which the pump beam strikes on the optical axis at the first plane and the microscope objective that focuses light on our sample at the final plane, the pump beam can be directed to enter the objective across a

wide range of angles without any change in the laser power incident on the sample that would otherwise be caused by clipping on the objective. Once through the objective, this range of angles translates to a range of positions on the sample that are then used to perform pump-probe spatial overlap scans by scanning the pump spot across the probe which has been centered on a flake. These scans are then performed at a variety of time delays and fit using a Gaussian (Fig. 6.4(b)). The fitting of these scans provides a measure of the width of the pump-polarized spin valley packet over time (Fig. 6.4(c)). As shown, there is no significant diffusion of the spin valley signal on the nanosecond time scale. Thus, it is determined that diffusion of spins away from the probe laser spot has negligible effect on the magnitude of the spin signal seen in the delay scans.

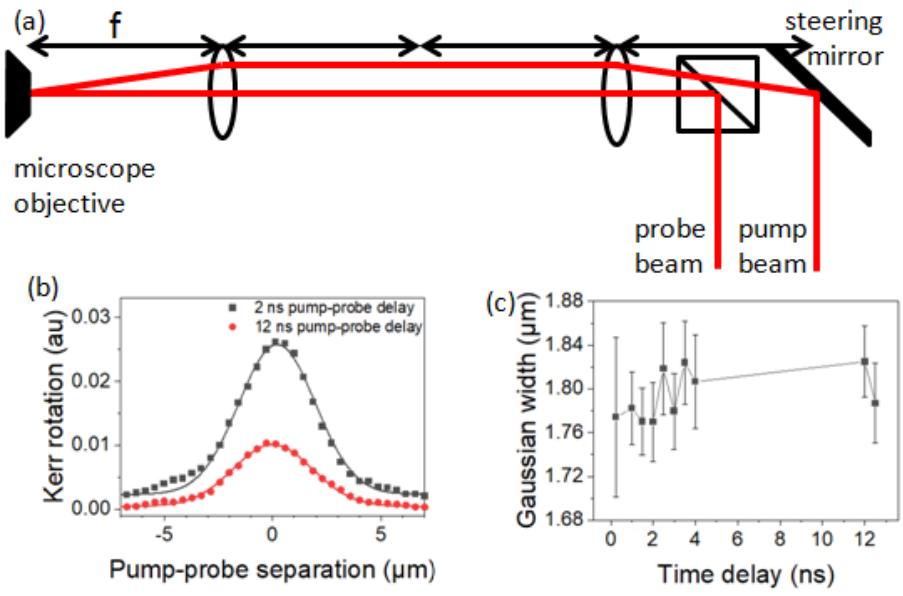

Figure 6.4 Pump-probe over lap data
(a) Two pump-probe overlap scans with the time delay fixed at 2 and 12 ns, with Gaussian fits to determine the width of the spin valley packet as a function of delay time. (b) Gaussian widths of the best-fit curves to multiple overlap scans such as those shown in (a) plotted as a function of delay time.

6.2.4 Conclusion

We have experimentally shown a nontrivial spatial dependence of the spin valley polarization in MOCVD-grown monolayer WSe_2, where, in large enough flakes, the excited polarization has increased magnitude near the edges. This occurs for both components of the bi-exponential fit with decay time constants of 3 ns and 80 ps. Interestingly, this is independent from the lifetime of the polarization which remains relatively constant across each flake. Spatially resolved microphotoluminescence and reflectivity measurements revealed constant behavior across each flake, implying that this does not result from inhomogeneity in the optical properties of WSe_2 near the edges of flakes. Utilizing the 4-f setup, pump-probe overlap scans were also employed at a range of delay times within the repetition rate of the laser and showed that there was no significant diffusion of the polarization over the time scales investigated in this study, eliminating diffusion as the cause of the increased spin valley polarization near the edges. These findings show that time-resolved Kerr rotation microscopy can be a useful tool for characterizing inhomogeneity of spin valley polarization in monolayer WSe_2 and other TMDs.

6.3 Laser degradation of samples with overlapping grains

The samples described previously are not the growth of MOCVD-grown samples we received nor are the individual grains entirely representative of that single growth. When growing single monolayer materials such as this, there are many knobs to tweak in the growth process that must be experimented with to achieve desirable results. Flow rates, precursor densities, times, and much else can be adjusted and all of these small adjustments will change not only the thickness of the growth, but also the sizes of individual grains and their densities. From the growth shown here specifically, the central area of the semiconductor wafer on which the sample was grown had a much higher density of flakes than on the edges. This gave us

essentially two regimes to experiment with: individual flakes which we have already discussed and the area near the center with the different flakes colliding during the growth process.

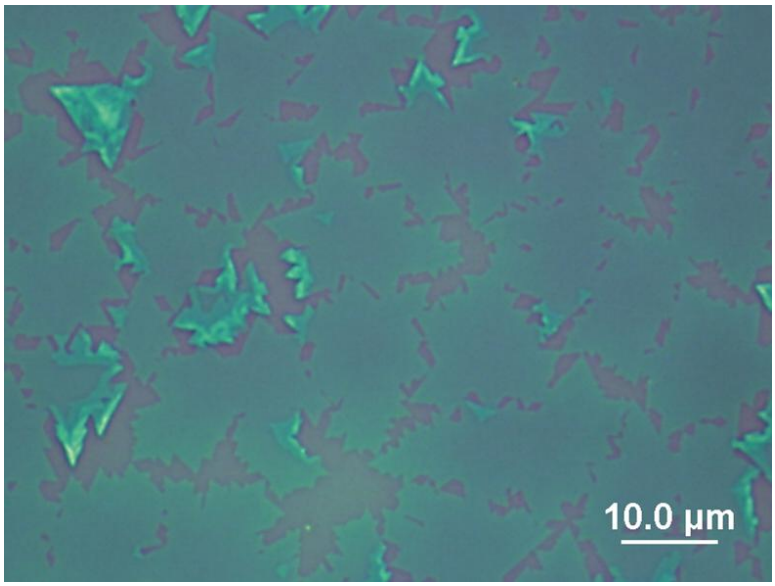

Figure 6.5 Higher density area of growth

The area with the higher density appears more desirable to work with at first glance, as it will be easier to position the laser beam on WSe_2 grains if there are more of them in the area. And indeed, the first measurements of this growth cycle were made there. However, there are downsides to an area such as this as well. Pictures displayed of this area are generally taken with a high quality optical microscope to provide the highest possible contrast between WSe2 and substrate. Once the sample is inside a cryostation and being viewed with a laboratory white light source and CCD, the contrast between WSe_2 and substrate decreases to nearly zero. In order to determine where exactly flakes are located, CCD exposure times of up to 1/3 of a second are often necessary. Because of the difficulty in seeing the samples, in an area like this with many random growths all crowded near each other, it can be a futile task to ensure that the laser spot

stays precisely positioned on the same part of the sample over repeated measurements. The sample drifting even one micron can cause a large change in the area that is being probed by the optical setup when working with these small length scales.

When the initial measurements were made on this sample, this small drift is what appeard to be occurring. The signal was decreasing approximately 25% over the course of 20 minutes of lab time. The first few sets of measurements that were usually taken on these samples were a few identical scans to ensure repeatability. Any change in signal over these repetitions will usually indicate something drifting or not quite settled in the experimental setup which will significantly impact future measurements. At the time of these measurements, the setup had been completed and in use for over a year, so if these sorts of irregularities existed it was usually a relatively easy fix, such as the optical coupling through a pinhole or the objective not being perfectly aligned. However even after checking the optics completely, repeated measurements still showed a steady decrease in signal, as plotted in Fig. 6.6.

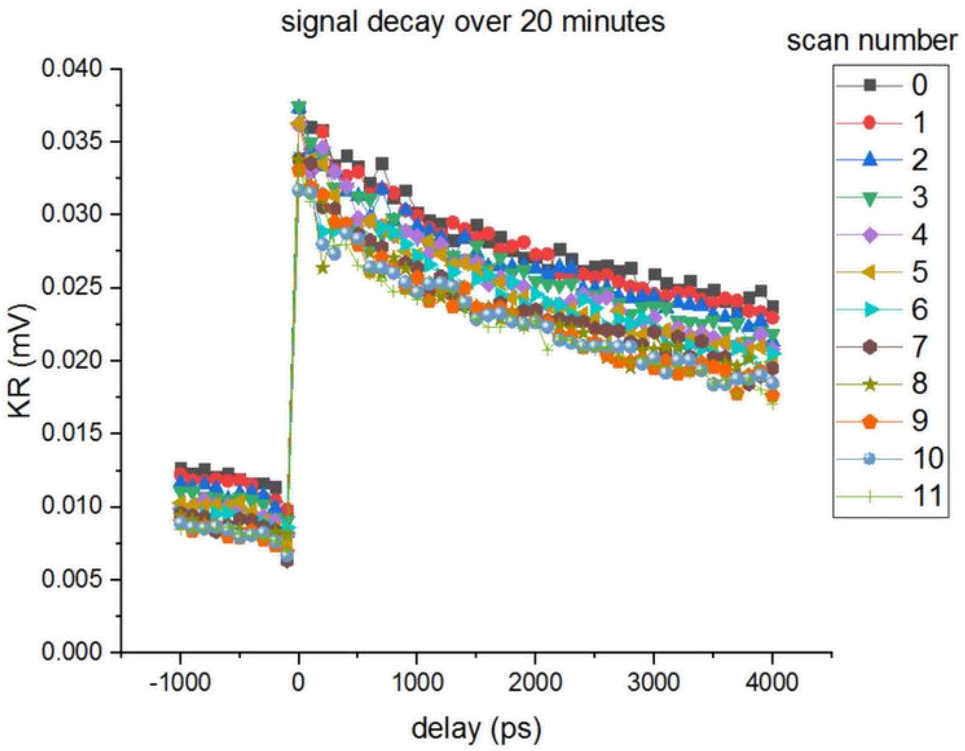

Figure 6.6 Multigrain sample decay.
This data was taken at 10 K, with 2.4 mW pump power and 0.4 mW probe power at 742.5 nm laser wavelength. It takes approximately 100 s of laboratory time to complete one delay scan, when taken quickly such as these scans.

With all the optics working correctly, the only option remaining is something changing with the sample. One possibility that I considered first was the sample slightly drifting such that the laser spot on the surface was either moving towards the edge of a grain or out of focus. After carefully observing the sample with noticable features (defects) on the substrate in view of the camera window, this drift did not appear to be occurring. This left two other possibilities: a poor vacuum seal on the cryostat allowing condensation to form on the sample or the laser is somehow causing the sample to degrade. Poor vacuum had been a problem previously in the setup, and the solution was a simple cleaning and re-greasing of the o-rings that acted as seals, so the procedure was completed and the vacuum working well with ease. However the signal decay

remained, which meant that the pump and probe striking the sample was causing it to degrade. To prove this theory, the laser was directed at the sample and a measurement was taken. Following this, the laser was blocked for a period of time before taking another identical measurement. We would then wait another period of time with the laser unblocked, fully striking the sample before taking a third measurement. This was repeated once again to ensure a full picture of what was happening.

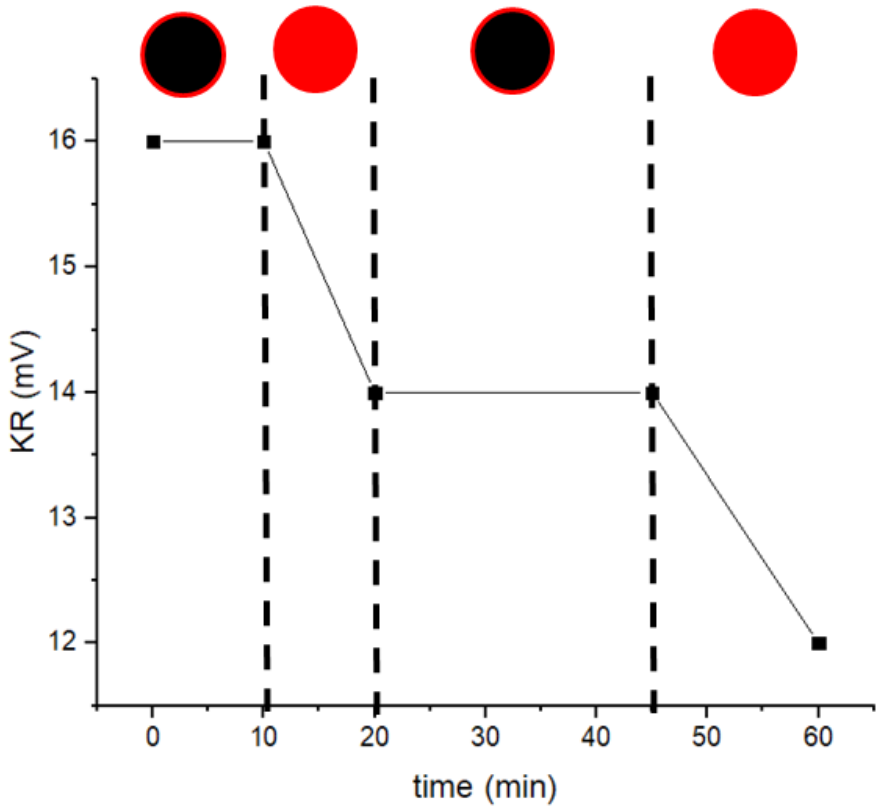

Figure 6.7 Sample degradation by laser light
Laser power vs. lab time, showing signal decreasing substantially when the laser is unblocked but a constant signal with when the laser is not allowed to strike the sample.

As seen in Fig. 6.7, the sample being degraded by laser light became abundantly clear after these measurements. After leaving the laser initially blocked for 10 minutes, no change in signal was seen. Ten minutes with the laser unblocked after this however caused more than a 10% decrease in signal. This is then seen again over the next hour, with no change in signal evident even when leaving the laser blocked for thirty minutes. These measurements demonstrated not only the degradation of these multigrain samples via laser light but also the robustness of the assembled experimental setup. This consistency over time was a welcome sight to see, as multi-part scans such as many of those shown in the previous section require hours of constant measurements to paint a full picture of the sample. This investigation into the signal decrease could be seen as the final test of our experimental apparatus being fully capable of everything it was designed to accomplish.

Chapter 7

Conclusion and Future Work

7.1 Conclusion

In this work, we have investigated the nontrivial spatial dependence of multiple optical measurements of WSe_2. These primarily utilized variations on Kerr rotation measurements, but also included photoluminescence and reflectivity measurements. We found that, while the Kerr amplitude of the spin valley polarization increased near the edges of the MOCVD-grown monolayer flakes studied, neither the photoluminescence amplitude nor the reflectivity scans showed any sign of this phenomenon. In the analysis of these measurements, we also found that the lifetime of the spin valley polarization in these flakes was independent of the position on the flake, similar to the photoluminescence and reflectivity measurements. In addition, these findings are repeatable across the first flakes studied as well as reproduced in another flake of comparable size, confirming that there is indeed a nontrivial spatial dependence of the spin valley amplitude in these flakes, despite the other measurements showing no pattern across the flake. This indicates some sort of effect or defect present at the edges of the flake, quite possibly from the grain boundaries that exist due to the six-sided star shape, that affects the amount of spins generated when struck with the laser pulse, without affecting other optical properties of the flake – namely the luminescence or its reflectivity.

In acquiring these findings, many other steps had to first be accomplished both in and outside of the lab to make the measurements possible. We looked at what went in to constructing the experimental setup used to perform these Kerr rotation and photoluminescence measurements on the incredibly small samples, as well as some of the day-to-day workings necessary to keep the setup running smoothly. The addition of the 4-f lens configuration to the experimental apparatus aided in the running of spatial pump-probe overlap scans used to study diffusion, as well as allowing for white light to be used to navigate our 3-um laser spot to the 10-um flakes present on the much, much larger (cm^2) sample surface. We also discussed efforts taken to add wiring to the cryostat and electrically contact these small samples in the clean room that may bear fruit in future endeavors to study spin drag and the valley Hall effect in similar materials.

7.2 Future Work

As always, with any research coming to an end under one graduate student's career, there are many and various paths that future work can take based off of what was accomplished during my time at the University of Michigan. There are many more studies I wish I had time to perform while I was here, as well as directions that I could have taken instead of what you read in this work.

As I concluded at the end of Chapter 6, a nontrivial spatial dependence is present in the samples studied without a concrete explanation for why this exists. One likely explanation for this pattern is the presence of grain boundaries near the edges of the flake (a flake with a single grain present would have a strictly triangular shape, instead of the six-sided star seen in these samples). However, it is impossible to say with certainty that this is the cause of the pattern seen when studying only flakes from this individual growth cycle. One possible direction to work off

of this in the future is to compare measurements taken from the MOCVD-grown samples with the spatial dependence of other WSe_2 samples, with mechanical exfoliation being the obvious choice. Repeating the measurements shown in Chapter 6 on an exfoliated sample should shine light on exactly what is happening in the measurements and is a promising topic for future study that could open up even more avenues of research.

Looking instead at Chapter 5, we have determined a useful technique to deposit electrical contacts consistently onto these samples to within a micron of where we wish them. This will hopefully allow for electrically contacted WSe_2 to be measured in the future, but, unfortunately the current liftoff technique used destroys the spin valley signal of our samples. It is my belief that the alignment and wire bonding processes described will be of use to future research endeavors, as only the liftoff technique needs to be adjusted to result in working devices. There are a few possibilities to be explored here, between finding a new liftoff technique to changing the process of deposition. Another option is to utilize a 'shadow mask.' This technique uses a mask with open holes where you want the contacts to be held over the sample during the metal deposition process, instead of photoresist being deposited on the sample. This has the advantage of not needing liftoff performed afterwards, which should leave researchers with a working sample afterwards. Unfortunately the exact alignment process here does not necessarily apply directly to shadow mask alignment, however I believe similar techniques may be applied with alignment markings on the sample and the mask.

When fully functioning electrically contacted samples are realized in our lab for these materials, many other avenues of research open up. The simplest of these are back gate dependent measurements with the gate having control over the carrier concentration of the sample. This can be used to adjust the majority carrier between electrons and holes and to study

the differences found in these two regimes. In addition, with source and drain contacts present on a flake, spin drag measurements become possible to perform. Spin drag measurements involve applying an electrical field to push the spin valley packet laterally after creation, which can give more insight into spin diffusion and their dynamics in these samples. Lastly, the spin valley Hall effect has been demonstrated in TMD samples, but to the best of my knowledge has only been seen in samples acquired through mechanical exfoliation. There may be differences present in the MOCVD-grown samples that would be of interest to future researchers. I am excited to see where this research branches off to in the future, and hopeful for what changes this may bring.

Bibliography

1. G. E. Uhlenbeck and S. Goudsmit, “Spinning electrons and the structure of spectra," Nat. 117, 264, (1926)
2. I. Zutic, J. Fabian, and S. Das Sarma, “Spintronics: Fundamentals and applications,” Rev. Mod. Phys. 76, 323 (2004)
3. S. A. Wolf, D. D. Awschalom, R. A. Buhrman, J. M. Daughton, S. von Molnar, M. L. Roukes, A. Y. Chtchelkanova, and D. M. Treger, “Spintronics: A Spin-Based Electronics Vision for the Future,” Science 294, 1488 (2001).
4. M. Baibich, J. Broto, A. Fert, F. Nguyen Van Dau, F. Petro, P. Etienne, G. Creuzet, A. Friederich, and J. Chazelas., “Giant Magnetoresistance of (001)Fe/(001)Cr Magnetic Superlattices,” Phys. Rev. Lett. 61, 2472 (1988)
5. G. Binasch, P. Grunberg, F. Saurenbach, and W. Zinn, “Enhanced magnetoresistance in layered magnetic structures with antiferromagnetic interlayer exchange," Phys. Rev. B 39, 4828 (1989)
6. S. Bhatti, R. Sbiaa, A. Hirohata, H. Ohno, S. Fukami, and S. N. Piramanayagam, “Spintronics based random access memory: a review,” Mat. Today 20(9), 530 (2017)
7. K. S. Novoselov, A. K. Geim, S. V. Morozov, D. Jiang, Y. Zhang, S. V. Dubonos, I. V. Grigorieva, and A. A. Firsov, “Electric Field Effect in Atomically Thin Carbon Films,” Science 306, 666 (2004)
8. S. Batalden and V. Sih, “Spatially-resolved measurements of spin valley polarization in MOCVD-grown monolayer WSe2,” Opt. Exp. 29, 17269 (2021)
9. “Graphene is not alone,” Nat. Nanotech. 7, 683 (2012)
10. K. F. Mak, C. Lee, J. Hone, J. Shan, and T. F. Heinz, “Atomically Thin MoS2: A New Direct-Gap Semiconductor,” Phys. Rev. Lett. 105, 136805 (2010)
11. A. Splendiani, L. Sun, Y. Zhang, J. Kim, C. Y. Chim, G. Galli, and F. Wang, “Emerging Photoluminescence in Monolayer MoS2,” Nano. Lett. 10, 1271 (2010)
12. G. Wang, C. Robert, A. Suslu, B. Chen, S. Yang, S. Alamdari, I. C. Gerber, T. Amand, X. Marie, and S. Tongay, “Spin-orbit engineering in transition metal dichalcogenide alloy monolayers,” Nat. Comm. 6, 10110 (2015)
13. X. Song, S. Xie, K. Kang, J. Park, and V. Sih, “Long-Lived Hole Spin/Valley Polarization Probed by Kerr Rotation in Monolayer WSe2,” Nano Lett. 16, 5010 (2016)
14. S. Manzeli, D. Ovchinnikov, D. Pasquier, O. V. Yazyev, and A. Kis, “2D transition metal dichalcogenides,” Nat. Rev. Mater. 2, 17033 (2017)
15. K. F. Mak, D. Xiao, and J. Shan, “Light-valley interactions in 2D semiconductors,” Nat. Photon. 12, 451 (2018)

16. T. Yan, S. Yang, D. Li, and X. Cui, “Long valley relaxation time of free carriers in monolayer WSe_2,” Phys. Rev. B 95, 241406 (2017)
17. F. Volmer, S. Pissinger, M. Ersfeld, S. Kuhlen, C. Stampfer, and B. Beschoten, “Intervalley dark trion states with spin lifetimes of 150 ns in WSe2,” Phys. Rev. B 95, 235408 (2017)
18. P. Dey, L. Yang, C. Robert, G. Wang, B. Urbaszek, X. Marie, and S. A. Crooker, “Gate-Controlled Spin-Valley Locking of Resident Carriers in WSe2 Monolayers,” Phys. Rev. Lett. 119, 137401 (2017)
19. T. Yan, J. Ye, X. Qiao, P. Tan, and X. Zhang, “Exciton valley dynamics in monolayer WSe2 probed by the two-color ultrafast Kerr rotation,” Phys. Chem. Chem. Phys. 19, 3176 (2017)
20. D. Xiao, G. B. Liu, W. Feng, X. Xu, and W. Yao, “Coupled Spin and Valley Physics in Monolayers of MoS2 and Other Group-VI Dichalcogenides,” Phys. Rev. Lett. 108, 196802 (2012)
21. X. Xu, W. Yao, D. Xiao, and T. F. Heinz, “Spin and pseudospins in layered transition metal dichalcogenides,” Nat. Phys. 10, 343 (2014)
22. L. Yang, N. A. Sinitsyn, W. Chen, J. Yuan, J. Zhang, J. Lou, and S. A. Crooker, “Long-lived nanosecond spin relaxation and spin coherence of electrons in monolayer MoS2 and WS2,” Nat. Phys. 11, 830 (2015)
23. W. T. Hsu, Y. L Chen, C. H. Chen, P. S. Liu, T. H. Hou, L. J. Li, and W. H Chang, “Optically initialized robust valley-polarized holes in monolayer WSe2,” Nat. Comm. 6, 8963 (2015)
24. T. Korn, S. Heydrich, M. Hirmer, J. Schmutzler, and C. Schuller, “Low-temperature photocarrier dynamics in monolayer MoS2,” Appl. Phys. Lett. 99, 102109 (2011)
25. D. Lagarde, L. Bouet, X. Marie, C. R. Zhu, B.L. Liu, T. Amand, and P. H. Tan, “Carrier and Polarization Dynamics in Monolayer MoS2,” Phys. Rev. Lett. 112, 047401 (2014)
26. E. J. McCormick, M. J. Newburger, Y. K. Luo, K. M. McCreary, S. Singh, I. B. Martin, E. J. Cichewicz Jr., B. T. Jonker, and R. K. Kawakami, “Imaging spin dynamics in monolayer WS2 by time-resolved Kerr rotation microscopy,” 2D Mater. 5, 011010 (2018)
27. X. Song, Optical Measurements of Spin/Valley Polarization in Transition Metal Dichalcogenides, PhD thesis, University of Michigan (2018)
28. J. M. Kikkawa and D. D. Awschalom, “Resonant Spin Amplification in n-Type GaAs,” Phys. Rev. Lett. 80, 4313 (1998)
29. T. Cao, G. Wang, W. Han, H. Ye, C. Zhu, J. Shi, Q. Niu, P. Tan, E. Wang, B. Liu, and J. Feng, “Valley-selective circular dichroism of monolayer molybdenum disulphide,” Nat. Commun. 3, 887 (2012)
30. C. Jin, J. Kim, K. Wu, B. Chen, E. S. Barnard, J. Suh, Z. Shi, S. G. Drapcho, J. Wu, P. J. Schuck, S. Tongay, and F. Wang, “On Optical Dipole Moment and Radiative Recombination Lifetime of Excitons in WSe2,” Adv. Func. Mat. 27, 1601741 (2017)
31. P. Rivera, K. L. Seyler, H. Yu, J. R. Schaibley, J. Yan, D. G. Mandrus, W. Yao, and X. Xu, “Valley-polarized exciton dynamics in a 2D semiconductor heterostructures,” Science 351, 688 (2016)

32. M. Y. Li, C. H. Chen, Y. Shi, and L. J. Li, “Heterostructures based on two-dimensional layered materials and their potential applications,” Mat. Today 19, 322 (2016)
33. J. Kim, C. Jin, B. Chen, H. Cai, T. Zhao, P. Lee, S. Kahn, K. Watanabe, T. Taniguchi, S. Tongay, M. F. Crommie, and F. Wang, “Observation of ultralong valley lifetime in WSe2/MoS2 heterostructures,” Sci. Adv. 3, e1700518 (2017)
34. J. Li, M. Goryca, K. Yumigeta, H. Li, S. Tongay, and S.A. Crooker, “Valley relaxation of resident electrons and holes in a monolayer semiconductor: Dependence on carrier density and the role of substrate-induced disorder,” Phys. Rev. Mat. 5, 044001 (2021)
35. K. Kang, S. Xie, L. Huang, Y. Han, P. Y. Huang, K. F. Mak, C. J Kim, D. Muller, and J. Park, “High-mobility three-atom-thick semiconducting films with wafer-scale homogeneity,” Nat. 520, 656 (2015)
36. K. F. Mak, K. He, J. Shan, and T. F. Heinz, “Control of valley polarization in monolayer MoS2 by optical helicity,” Nat. Nanotechnol. 7, 494 (2012)
37. Z. Wu, W. Zhao, J. Jiang, T. Zhen, Y. You, J. Lu, and Z. Ni, J. “Defect Activated Photoluminescence in WSe2 Monolayer,” Phys. Chem. C 121, 12294 (2017)
38. J. Huang, T. B. Hoang, T. Ming, J. Kong, and M. H. Mikkelsen, “Temporal and spatial valley dynamics in two-dimensional semiconductors probed via Kerr rotation,” Phys. Rev. B 95, 075428 (2017)
39. H. R. Gutiérrez, N. Perea-López, A. L. Elías, A. Berkdemir, B. Wang, R. Lv, F. López-Urías, V. H. Crespi, H. Terrones, and M. Terrones, “Extraordinary Room-Temperature Photoluminescence in Triangular WS2 Monolayers,” Nano Lett. 13, 3447 (2013)
40. W. Bao, N. J. Borys, C. Ko, J. Suh, W. Fan, A. Thron, Y. Zhang, A. Buyanin, J. Zhang, S. Cabrini, P. D. Ashby, A. Weber-Bargioni, S. Tongay, S. Aloni, D. F. Ogletree, J. Wu, M. B. Salmeron, and P. J. Schuck, “Visualizing nanoscale excitonic relaxation properties of disordered edges and grain boundaries in monolayer molybdenum disulfide,” Nat. Commun. 6, 7993 (2015)